Arabian Journal for Science and Engineering
https://doi.org/10.1007/s13369-025-10426-0

RESEARCH ARTICLE-MECHANICAL ENGINEERING

Enhancing Fluidic Oscillator Performance for Improved Outlet Jet Frequency and Reduced Pressure Drops by the Adjoint method

Hossein Jabbari[1] · **Ali Esmaeili**[1]

Received: 19 October 2024 / Accepted: 2 July 2025

Abstract
In this study, the efficiency of active flow-control devices was targeted by redesigning a vortex-based fluidic oscillator so that higher outlet jet-flow frequency could be obtained with lower internal pressure drop. In particular, these two are key metrics: higher oscillation frequencies enable more effective flow manipulation, while lower pressure losses reduce energy consumption. However, improvements in these performance metrics have traditionally been pursued through trial-and-error design iterations, which lack precision and require substantial computational effort. In this work, a gradient-based adjoint sensitivity analysis was employed as a design tool to systematically guide geometric modifications of the Coanda surface and feedback channel. The aim was to increase the jet oscillation frequency while reducing internal pressure losses. Two-dimensional unsteady Reynolds-averaged Navier–Stokes simulations using the Shear Stress Transport turbulence model were conducted to evaluate the proposed design modifications, and the computational results were validated against data from prior studies. The sensitivity-guided optimization indicated that subtle geometric changes can yield substantial benefits: for example, increasing the Coanda surface angle by 12° was found to raise the jet oscillation frequency by approximately 70% while lowering internal pressure losses by approximately 18% relative to the original design. It is demonstrated that these targeted, sensitivity-based modifications improve vortex dynamics within the oscillator and significantly enhance overall performance. Phase-portrait and spectral analyses were employed to confirm stable harmonic behavior and to reveal enhanced vortex coherence within the oscillator. Overall, this study deepens the understanding of fluidic oscillator behavior and provides practical guidelines for designing more efficient active flow control devices across a range of applications such as thermal-management applications.

Keywords Feedback fluidic oscillator · Sweeping jet · Vortex-based · Sensitivity analysis · Adjoint method · Numerical · Higher momentum flux · Unsteady Reynolds-averaged Navier–Stokes

1 Introduction

Recent developments in vortex-based feedback fluidic oscillators have garnered considerable attention due to their unique properties and versatility across diverse applications [1, 2]. Among various designs, the sweeping jet oscillator has been prominently featured in recent research, particularly for its use of a feedback channel that facilitates the generation of oscillating jet flows [3]. This type of oscillator epitomizes the foundational advancements in the field, setting the stage for further innovative applications. The sweeping jet oscillator is distinguished by its capacity to generate self-induced oscillating jets without the need for mechanical parts. This is achieved through sophisticated internal flow dynamics, which also enable the creation of transverse sweeping jets [4]. The adaptability of these oscillators to operate across a wide range of frequencies is especially critical, allowing customization to meet specific operational demands effectively. Moreover, the principle of distributed momentum addition, inherent to fluidic oscillators, plays a pivotal role in enhancing their application within the domains of fluid mechanics and heat transfer.

✉ Ali Esmaeili
aliesmaeili@ferdowsi.um.ac.ir

Hossein Jabbari
hossein.jabbari@mail.um.ac.ir

[1] Mechanical Engineering Department, Faculty of Engineering, Ferdowsi University of Mashhad, Mashhad, Iran

Published online: 08 August 2025

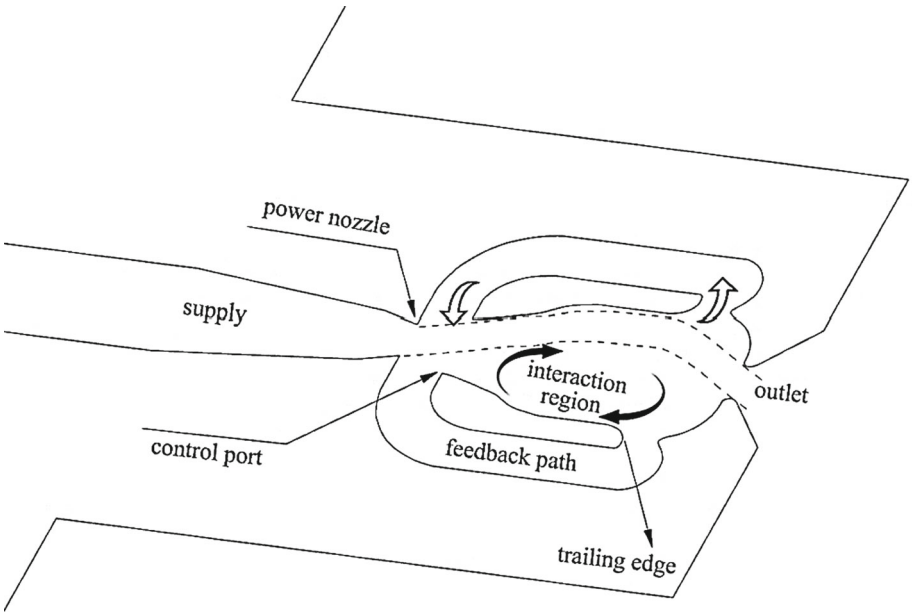

Fig. 1 Schematic of the inlet, feedback channels, mixing chamber, and diffuser. The curved Coanda surface is indicated to show how self-induced jet oscillations are generated

1.1 Basic Concept

Fluidic oscillators, integral to various engineering applications, operate based on the principle of flow instabilities that facilitate the generation of a periodically oscillating jet. This oscillation is self-induced and sustained by inherent instabilities within the device, characterized by a steady input of pressurized fluid transforming into a dynamic output action [5, 6]. The quintessential feedback fluidic oscillator, as detailed in Fig. 1, includes several critical components: the primary jet channel, which serves as the central pathway for introducing pressurized fluid and dictates the initial direction and flow characteristics of the jet; twin control jet channels positioned adjacent to the primary jet channel, which play a pivotal role in the oscillation mechanism by selectively alternating the flow attachment to the sidewalls and detachment therefrom, thereby regulating the direction and periodicity of the jet oscillation; and the main diffuser, which acts as the emission point for the oscillating jet, stabilizing and directing the flow as it exits the oscillator, contrary to misconceptions that it serves to regain pressure, making it suitable for targeted applications [7, 8]. The Coanda effect is instrumental in the functionality of fluidic oscillators, describing the tendency of the jet to adhere to a contiguous surface, thereby enabling the control channels to effectively manipulate the jet's attachment to the sidewalls; this mechanism is critical for maintaining the self-induced oscillation of the jet without mechanical intervention [9, 10].

1.2 Application

Significant strides have been made in understanding the fluid mechanics governing fluidic oscillators and optimizing their design for enhanced performance. For instance, studies have demonstrated their effectiveness in flow separation control [11, 12], such as full-scale vertical tails [13], and simple-hinged flaps [14], as well as over airfoils [15]. Furthermore, fluidic oscillators have been utilized to modulate fuel and air mixing, thereby improving efficiency and reducing emissions [16]. Additionally, their application in reducing the aerodynamic drag of bluff bodies, like the Ahmed body, showcases their utility in automotive engineering [17]. For instance, the notable investigation by [13] highlighted the substantial impact of fluidic oscillators on the lateral force of an aircraft's vertical tail, where a modified oscillator configuration led to a 20% increase in suction pressure and enhanced lateral stability. This finding underscores the potential of tailored oscillator designs to significantly influence aerodynamic performance metrics.

Beyond aerodynamic applications, fluidic oscillators have proven valuable in energy harvesting scenarios, exploiting the flow-induced oscillations to convert the kinetic energy of fluid into strain energy in a piezoelectric structure, detailing the influence of fluid velocity and beam placement on power output and voltage optimization [18]. Their use in precision measurement of mass flow rates in pipelines demonstrates their adaptability across different scales and conditions, with effective operation across a Reynolds range from 300 to 50,000 [19, 20]. Here, the technology's capacity to derive flow meter characteristics through the evaluation of static

pressure fluctuations is a testament to its versatility and precision.

Moreover, fluidic oscillators have demonstrated their utility in specific scenarios, such as enhancing heat transfer in gas turbine blades [21–23], even when compared to synthetic jets with temporal oscillations [24] or when employed as compressible oscillating jet [25]. Hossain et al. [22] conducted both numerical and experimental investigations that highlighted the effectiveness of fluidic oscillators for cooling plates subjected to high-temperature flows, particularly in gas turbine applications, where these devices demonstrated superior heat transfer coefficients compared to conventional methods. Additionally, these devices offer advantages across diverse fields, including aerodynamic drag reduction [26, 27], noise control [28], creation of uniform nanofluids in thermosiphons [29], enhancement of air and natural gas mixing in dual-fueled diesel engines [30], and improved irrigation flow in root canals for enhanced microorganism removal [31]. Each application benefits from the oscillator's ability to generate high-momentum, coherent jet streams that can be precisely directed due to the Coanda effect, a fundamental fluid dynamic principle that ensures fluid adherence to contoured surfaces, thus allowing for controlled manipulation of flow trajectories.

The physics underlying these enhancements involves complex interactions between the fluid properties and the oscillator geometry, particularly how modifications to the Coanda surface impact the flow dynamics. Over the past five years, substantial progress has been made in optimizing the performance and expanding the applications of fluidic oscillators, especially increasing the outlet jet frequency. For instance, study by Hussain et al. [32] demonstrated that integrating rectangular ribs on the Coanda surface of a fluidic oscillator significantly enhances flow performance. Specifically, they found that increasing the aspect ratio of the ribs from 0.64 to 1.56 elevated the jet oscillation frequency from 355 to 820 Hz and reduced the pressure drop by 22%. These modifications were attributed to the formation of a separation bubble in the mixing chamber, which effectively modulated the oscillatory characteristics of the jet. Similarly, [33] investigated the sensitivity of a fluidic oscillator to internal geometry modifications, focusing on the feedback channel and mixing chamber. Their experimental study revealed that localized changes in the Coanda surface shape could transition the external flow regime from bifurcated to homogeneous, thereby affecting jet deflection angles and sweeping frequency. Notably, they observed that actuator designs with straight Coanda surfaces performed comparably to traditional curved geometries, suggesting potential simplifications in oscillator design without compromising performance.

In another study, scholars [34] conducted a numerical characterization of jet oscillation frequencies in sweeping jet actuators using 3D-URANS simulations. They established a linear relationship between jet oscillation frequency and the time-averaged exit nozzle Mach number ($f = 511.22\,M + 46.618$, $R2 = 0.97$), and confirmed that the Strouhal number remained nearly constant ($St \approx 0.0131$) across various Mach numbers in subsonic flows. This study provided a computationally efficient model for predicting oscillation characteristics, facilitating the design and optimization of fluidic oscillators. In the realm of novel oscillator designs, Yang et al. [35] introduced the sweeping-vortex fluidic oscillator (SVFO), which exploits unique feedback properties and vortex interactions to achieve low-frequency oscillations. Their CFD analysis revealed that increasing the overall width of the oscillator could enhance oscillation frequency by up to 87%, while geometric parameters such as sweeping chamber height and vortex chamber outlet diameter significantly affected pressure pulse amplitudes. These findings underscore the intricate interplay between geometric configurations and oscillatory behavior in fluidic oscillators. Furthermore, [36] compared the performance of fluidic oscillators and sweeping jets (SJs) as unsteady actuators for flow control at high Reynolds numbers. Their numerical simulations indicated that SJs could achieve higher oscillation frequencies with lower power requirements compared to traditional fluidic oscillators, making them more efficient for applications like aerodynamic performance enhancement and combustion control.

Another pertinent study by Joulaei et al. [37] investigated the impact of geometric scaling on the heat transfer performance of fluidic oscillators. Using URANS simulations with a k-ω SST turbulence model, they demonstrated that reducing the scale factor of the oscillator geometry increased the oscillation frequency and enhanced the Nusselt number by up to 13%, thereby improving cooling efficiency. This research highlighted the potential of geometric optimization in tailoring fluidic oscillator performance for thermal management applications. Furthermore, echoing this computational approach, Meng et al. [38, 39] embarked on a numerical simulation to scrutinize the enhancements in performance and flow control within an axial compressor achieved through the incorporation of an oscillator. The studies delved into several critical aspects, including the oscillator's placement, the orientation of the output jet relative to the compressor blades, and its oscillation frequency. These factors are pivotal as they directly influence the effectiveness and efficiency of the compressor's operation, guiding the optimization of the device's configuration for maximal performance enhancement. Chen et al. [40] demonstrated that the performance of sweeping jets in managing afterbody vortices is critically dependent on the jet's momentum coefficient, which in turn influences the dimensions and behavior of vortices and their separation from the base, ultimately affecting the pressure distribution on the surface.

Moreover, Alikhassi et al. [18] succeeded in transforming fluidic kinetic energy into tension energy within a piezoelectric structure, employing a fluidic oscillator to achieve this conversion. The innovative use of fluidic oscillators in this context opens up new avenues for energy harvesting and smart material applications. Addressing the importance of internal geometrical configurations, a series of studies including experimental work by Wen et al. [41] reported that altering the widths of the inlet wedge (W1), mixing chamber (W2), and exit throat (W3) normalized by the inlet throat width (W0) directly influenced the oscillation frequency and jet spreading angles. For instance, an inlet wedge width ratio (W1/W0) of 2 resulted in a proportional increase in both jet spreading angle and oscillation frequency, highlighting the critical role of inlet geometry in controlling oscillator performance.

CR45Despite these significant advancements, several critical gaps persist in the literature. Notably, while numerous studies have explored the effects of geometric modifications on oscillator performance, there remains a lack of comprehensive sensitivity analyses by employing Adjoint method that systematically and mathematically evaluate the influence of localized geometric changes within the feedback channels on global performance metrics such as oscillation frequency, pressure fluctuations, and jet deflection angles. This study addresses these gaps by employing Adjoint method a novel sensitivity-based methodology to examine the internal flow dynamics of feedback channels with strategic geometric modifications. Traditionally, the approach has been to uniformly widen these channels or simplistic geometric alterations, the present approach employs a systematic sensitivity analysis to identify and quantify the impact of specific geometric features on oscillator performance. This includes the integration of diffuser-like shapes within the feedback channels to modulate local pressure drops and adjust fluid dynamics, thus enhancing system stabilizing oscillation frequencies [42], rather than merely increasing channel widths. Contrary to earlier assumptions that a diffuser completely regains pressure, it primarily helps in reducing pressure drop intensity, which in turn stabilizes outlet frequency and overall system resilience. The used methodology introduces several configurations of feedback channel widths and examines their effects through rigorous post-processing techniques. These techniques include phase portrait circuit analysis and vortex structure characterization, in conjunction with high-fidelity computational models, assessments of pressure fluctuation intensity, and evaluations of jet deflection angles, streamlines and dynamic flow characteristics. Through these analyses, it is offered a comprehensive view of how these geometric alterations can optimize fluidic oscillator performance across various operational conditions.

2 CFD Approach

2.1 Defining the Geometry and Considering Design Factors

As shown in Fig. 2, the computational domain is two-dimensional, with an oscillating jet originating from a single outlet nozzle situated to the left of the origin. In this context, the horizontal axis (x) corresponds to the primary jet flow direction, while the vertical axis (y) represents the spanwise direction. In this study, simulations were conducted on the SWJ with an outlet throat width of 6.35 mm. To enhance the experimental setup, a semi-circular region with a radius of 635 mm was introduced at the nozzle exit plane. Additionally, a two-dimensional straight channel with a height of 16.21 mm into the actuator inlet to ensure a fully developed flow in the upstream section of the converging nozzle was integrated. Due to the significance of specific points, namely 6, 0 mm, (x, y), located at the nozzle outlet, these points were emphasized when reporting vital findings, including frequency analyses. Additional details about the system's configuration and specifications can be found in Ref. [43], and Table 2.

In the absence of feedback channels, the jet flow remains symmetric, resulting in the absence of oscillations. However, the introduction of feedback channels, coupled with careful selection of appropriate design parameters, induces uneven growth and shrinkage of vortices, leading to oscillation formation [44]. Figure 2 provides a schematic representation of the modified SWJ actuator designs, highlighting variations superimposed on the reference geometry. Detailed information on this model can be found in Ref [43]. The primary focus of these geometric modifications centers on the feedback channel width.

The key design factors for the modified oscillator include the following:

- In the design of the feedback channel, it is crucial to ensure that the throat at the trailing edge is larger than its inlet throat. This particular configuration results in an increased flow rate within the feedback channel, leading to the intensification of flow after oscillation occurs. When the throat at the trailing edge is appropriately sized, it creates a pressure differential between the secondary and primary chambers, enabling oscillation to take place and maintaining a consistent outlet frequency. Conversely, if the throat at the trailing edge is smaller than the inlet throat, it can prevent the effective recovery of pressure intensity in the jet core, leading to disruptions in the outlet jet. It is, therefore, imperative to carefully balance and optimize the throat sizes to ensure proper flow dynamics and stable oscillation behavior in the system.
- This modification has been carefully executed while ensuring a consistent distance between the inlet throat and

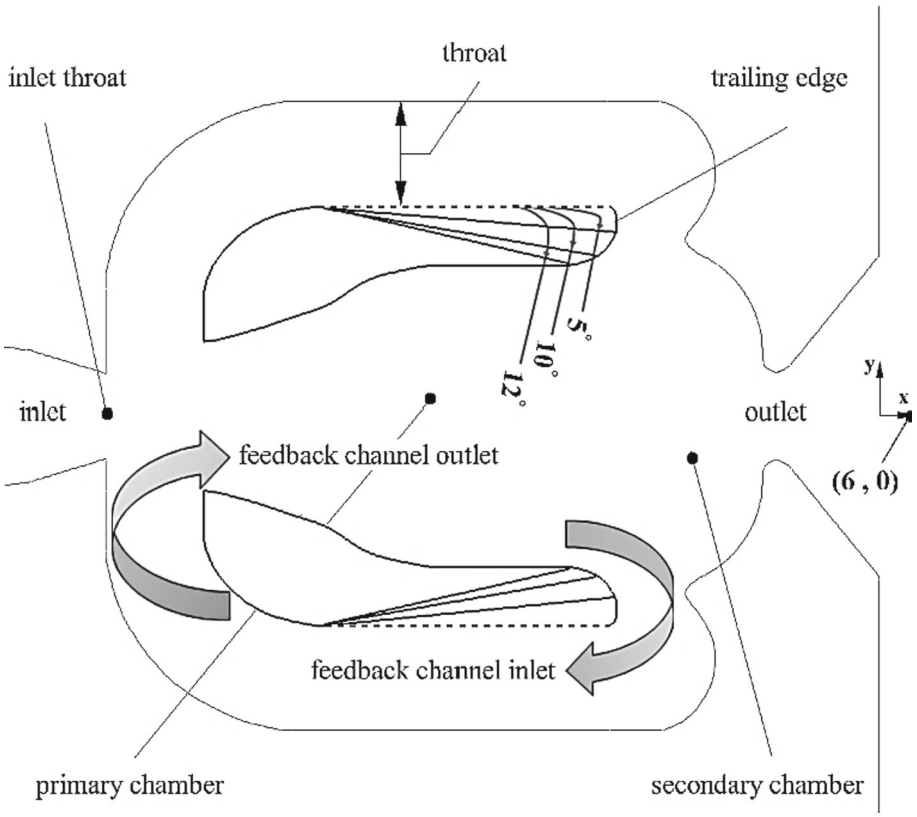

Fig. 2 Comparisons between the baseline curved SWJ and three variants (5°, 10°, 12°) with altered Coanda surfaces and trailing edge

Coanda surfaces. This deliberate adjustment holds significance as both the positions of the inlet throat and the adjacent feedback outlet wall substantially influence flow characteristics. Notably, previous observations [33] have indicated that a reduction in the distance between the inlet throat and Coanda surfaces leads to a decrease in outlet frequency.

2.2 Governing Equations

To investigate the flow oscillations occurring both inside and outside the SWJ actuator, a numerical approach was adopted. Specifically, the finite volume method was employed to solve the 2D URANS equations, which govern the conservation of mass and momentum in the system. This CFD technique allows for a comprehensive examination of the flow patterns, offering insights into the transient dynamics of the oscillator [45]. While RANS predictions offer several advantages for turbulent flows, it is essential to acknowledge their limitations. RANS equations describe flows statistically, relying on velocity fields and time-averaged pressure. Consequently, this approach fails to distinguish between quasiperiodic large-scale structures and turbulent chaotic small-scale structures within the flow field [46, 47]. This limitation becomes particularly problematic when both phenomena coexist in the flow field. To address these challenges and attain equilibrium between precision and computational effectiveness, the URANS analysis was chosen for the present flow investigation. It offers a middle ground, achieving equilibrium between precision and computational effectiveness when examining flow phenomena within the fluidic oscillator [46, 48].

2.3 Numerical Scheme and Turbulence Model

To model turbulence closure, the shear-stress transport (SST) $k-\omega$ turbulence model [49] is employed. The simulations are performed with air as the working fluid, and the molecular viscosity is determined using Sutherland's law, which offers a method to evaluate the molecular viscosity of air as a function of temperature:

$$\mu_T = \mu_0 \left(\frac{T}{T_0}\right)^{3/2} \left(\frac{T_0 + S}{T + S}\right), \quad \left(\mu_0 = 1.716 \times 10^{-5} kgm^{-1}s^{-1}, \; T_0 = 273.16k, \; S = 110.56K\right) \tag{1}$$

where μ_0, T_0 and S reference viscosity, reference temperature, and effective temperature, respectively. The selection of the $k-\omega$ turbulence model for this study was driven by its

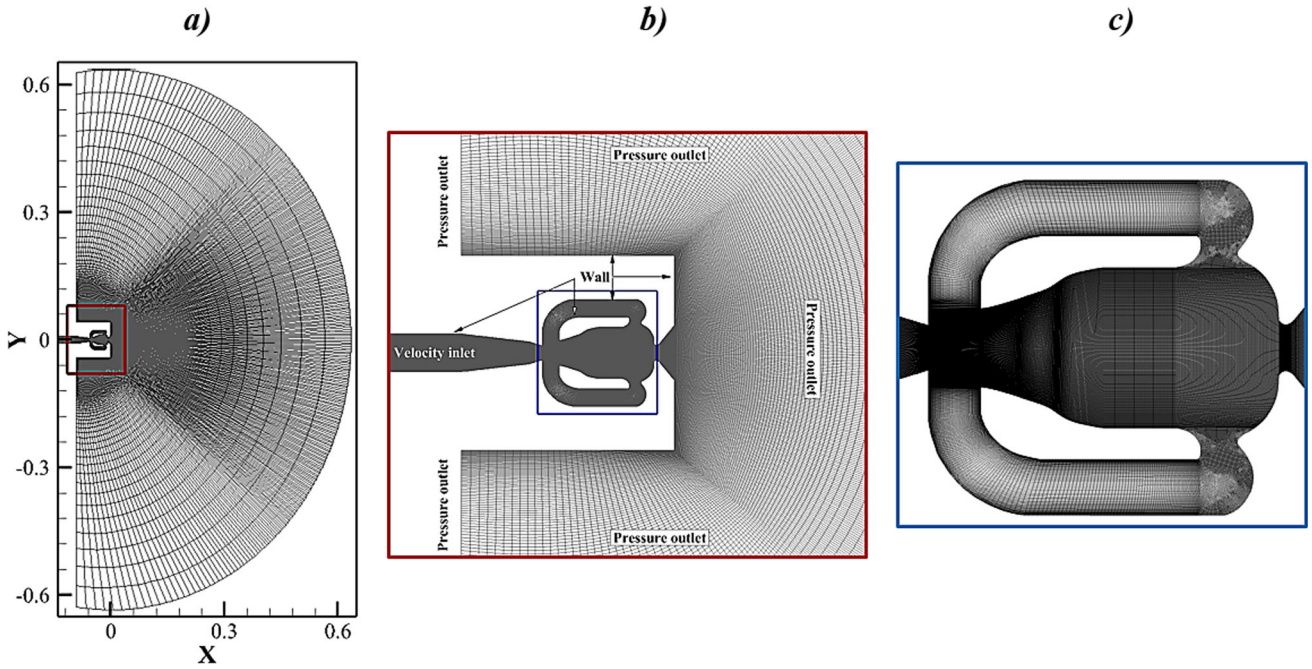

Fig. 3 Computational mesh with 889.207 $\times$ 10^3 elements; **a** Computational domain (XY plane) and **b** & **c** close-up views of the SWJ mesh, and boundary conditions

well-documented proficiency in capturing the near-wall flow behavior, which is of paramount importance in fluidic oscillator analysis. This model is renowned for its robustness and accuracy in simulating boundary layer flows with adverse pressure gradients, as seen in Coanda-effect-dominated fluidic oscillators. Moreover, the $k-\omega$ model's formulation inherently includes modifications for low-Reynolds-number effects, which allows for the precise simulation of turbulent kinetic energy and specific dissipation rates close to the walls. This level of detail is crucial for understanding the complex interactions between the jet and the Coanda surface, as well as the subsequent vortex formations and oscillations. It is noteworthy that the turbulent Prandtl number plays a significant role in turbulence models, it is set on 0.72, based on previous study [34].

To discretize the RANS equations with second-order accuracy, the control volume method is employed. This numerical approach is well-suited for analyzing turbulent flows and offers efficient and accurate results, particularly in two-dimensional cases. It also exhibits potential for addressing three-dimensional problems. For unsteady calculations, the pressure-implicit with splitting of operators (PISO) algorithm is utilized. This algorithm, combined with a second-order fully implicit scheme for time integration, ensures robust and stable simulations of transient flow phenomena. The PISO algorithm efficiently manages the coupling between pressure and velocity fields, enabling accurate and reliable unsteady simulations. By harnessing the control volume method for spatial discretization and the PISO algorithm for unsteady calculations, the numerical solver demonstrates its capability to handle complex turbulent flows and transient flow phenomena. The second-order accuracy of the discretization method significantly contributes to the overall precision of the simulations, rendering it a suitable choice for a wide range of fluid flow problems.

2.4 Grid Generation and Boundary Conditions

The numerical simulation relies on a meticulous grid generation and thoughtful boundary condition considerations, both of which play a pivotal role in revealing the intricate flow patterns and behavior within the modified fluidic oscillator. For the simulation, a combination of structured and unstructured grids was employed near and away from the walls, respectively (Fig. 3).

As illustrated in Fig. 3-b, the majority of the grid was structured to enhance result quality and reduce computational errors, enabling a thorough evaluation of the mesh type's impact on the solution. To accurately capture the completely oscillatory flow, characterized by numerous harmonic vortices and recirculating patterns, uniform fine grids for the entire oscillator selected almost. A considerable external space was thoughtfully included to facilitate a smooth flow convergence toward ambient pressure. In this research, air served as the working fluid, and the boundary conditions were configured with the inlet velocity at the nozzle and ambient pressure at the outlet. Figure 3 provides an overview of the computational domain and grids for both the interior and

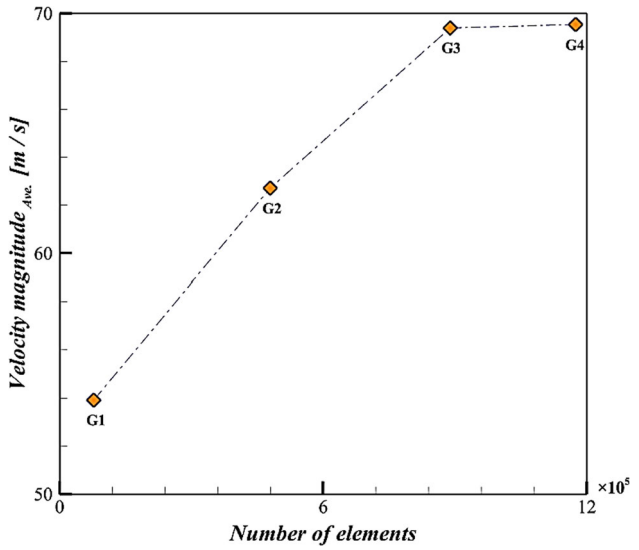

Fig. 4 Comparison of averaged velocity magnitudes obtained from coarse, medium, and fine grids, demonstrating minimal variation and confirming both grid convergence and the independence of the selected mesh resolution

exterior of the fluidic oscillator. To ensure a seamless transition of the sweeping jet to ambient pressure, the ambient pressure boundary was positioned at a significant distance from the nozzle exit.

2.5 Grid and Time Step Independence Study

Ensuring the accuracy and reliability of numerical simulations necessitates a meticulous grid independence and time step analysis. In this study, as shown in Fig. 4 a comprehensive evaluation of four distinct grid configurations was conducted to ascertain the optimal mesh size that balances computational efficiency with solution accuracy. The selected parameter for this evaluation was the average velocity magnitude at the critical point (6, 0), a location identified for its significant influence on the oscillatory behavior of the fluidic oscillator and tends to converge toward an asymptotic value as the number of elements increases. Each grid was generated using a structured mesh approach, ensuring high-quality element distribution around regions of expected high gradient, particularly near the Coanda surfaces and within the feedback channels. The mesh quality was assessed based on orthogonality and skewness, with all configurations maintaining orthogonality above 87%, adhering to best practices in CFD mesh generation.

As depicted, both Grid-3 and Grid-4 exhibit negligible differences in average velocity magnitude, indicating that Grid-3 is sufficiently fine to capture the essential flow dynamics with a minimal increase in computational cost. Consequently, Grid-3 (889,207 elements) and Grid-4 (1,174,038 elements)

Table 1 Resonance frequency for different grid

	Grid 3 (889,207)	Grid 4 (1,174,038)
Resonance frequency [Hz] (mass flow rate = 0.010 [lb/s])	258.17	259.04

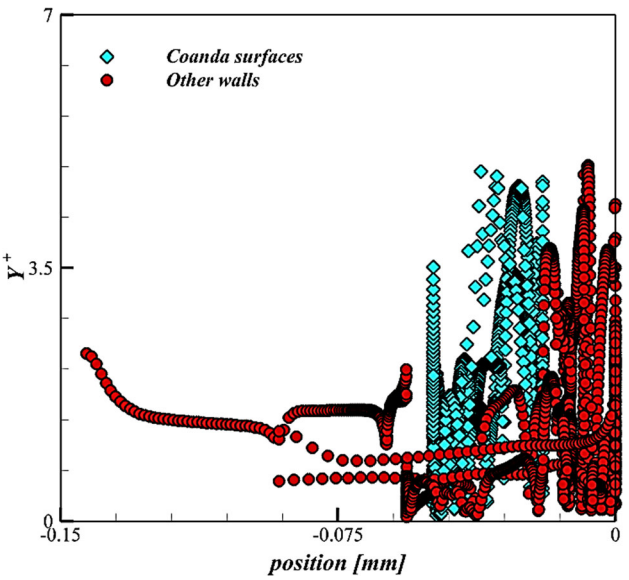

Fig. 5 Dimensionless wall distance (y^+) plot on the Coanda surfaces and nearby walls, ensuring adequate boundary-layer resolution for the k−ω SST model

were deemed adequately independent, ensuring mesh autonomy for subsequent simulations.

To further validate mesh independence, key performance metrics, oscillation frequency and pressure distribution, are compared across Grid-3 and Grid-4. Table 1 summarizes the results derived from FFT analysis of the velocity time series at the actuator exit. The oscillation frequencies of Grid-3 and Grid-4 differ by only 0.3%, while the pressure drops exhibit only marginal differences. These discrepancies are within acceptable numerical tolerances, affirming that Grid-3 provides an accurate representation of the flow without the necessity for further mesh refinement.

Maintaining appropriate Y^+ values is critical for accurately resolving boundary layer effects. Figure 5 presents the distribution of Y^+ values across all wall surfaces for Grid-3. This maintains Y^+ values below 5, satisfying the requirements for wall-resolved turbulence modeling with the $k-\omega$ *SST* turbulence model employed in our simulations. This ensures that near-wall flow phenomena are accurately captured without necessitating wall function approximations.

For all cases, a time step of 0.00001, $\Delta t=10^{-5}$s was utilized in the numerical simulations. This time step was

Table 2 Overview of solution conditions for the present work and Kara 2015 [43]

Solution conditions	Numerical solution of Kara 2015 [43]	Present numerical solution
Turbulence model	(SST) k−ω	(SST) k−ω
Inlet velocity [m/s]	37.2, 55.8, 74.4	37.2, 55.8, 74.4
Inlet total temperature [K]	298.8, 299.7, 300.9	298.8, 299.7, 300.9
Inlet total pressure [Pa]	102,147.5, 103,182.3, 104,643.5	102,147.5, 103,182.3, 104,643.5
Mass flow rate [lb/s]	0.010, 0.015, 0.020	0.010, 0.015, 0.020
Mass flux $[kg/m^2\ s]$	44.067, 66.100, 88.133	44.067, 66.100, 88.133
Grid type	Structured–Unstructured	Structured–Unstructured
Grid elements	1,113,193	889,207
Max.Y^+	1–5	< 5 (Fig. 5)

thoughtfully selected as it demonstrated sufficient accuracy in capturing the oscillation frequency. It is noteworthy that this specific time step has been validated in the reference [43], against which the current results were compared.

2.6 Numerical Verification

To validate the numerical simulations done in the current study and assess their performance, a conventional fluidic oscillator with specific Coanda surfaces was selected. Numerical simulations of the flow inside this fluidic oscillator were conducted, and the outcomes obtained were compared with the numerical findings reported by Kara [43]. The geometry and solution conditions employed in our study were explained as detailed in Table 2.

The validation of the numerical setup, including boundary conditions and grid resolution, was thoroughly examined and is depicted in Fig. 6. Figure 6 a displays a comparative analysis of average velocity magnitudes from the current simulations and prior numerical data provided by Kara et al. [43]. This comparison reveals a consistent increase in velocity magnitude with elevated mass flow rates, affirming the robustness of the present simulations conducted using the URANS framework and the $k-\omega$ *SST* turbulence model. Meanwhile, Fig. 6 b contrasts these results with experimental data from Vasta et al. [50], focusing on the velocity time-series at the sampling point (6, 0), located at the throat of the SWJ actuator exit nozzle as shown in Fig. 2. Here, the data exhibits well-defined, periodic oscillations.

Additionally, Table 3 offers a comparative analysis of oscillation frequencies between the current simulations and the findings by Kara et al. [43]. This comparison indicates a close agreement, thereby validating the methodological approach. This extensive validation process not only corroborates our numerical predictions but also reinforces the value of the Coanda surface modifications in advancing the technology of fluidic oscillators for more efficient flow control.

Table 3 Resonance frequency for the current study and Kara 2015 [43] at sampling point (6, 0)

	Numerical solution of Kara [43]	Present numerical solution	Percentage error %
Resonance frequency [Hz] (mass flow rate = 0.010 [lb/s])	251.9	258.17	∼ %2.4

2.7 Sensitivity Analysis

The adjoint method is instrumental within the Navier–Stokes framework, serving as a sophisticated analytical tool for assessing the sensitivity of fluid flows to changes in design parameters. Grounded in the principles of variational calculus and the strategic use of Lagrange multipliers, this method transforms the complex dynamics of fluid systems into a more manageable optimization problem. The essence of the adjoint approach lies in constructing an adjoint equation tailored to specific flow scenarios. This equation helps quantify the effects of variations in flow parameters on a designated objective function, such as pressure drop, enabling a precise gradient analysis with respect to various design variables like surface curvature or boundary conditions. By facilitating this kind of detailed sensitivity analysis, the adjoint method allows scholars to anticipate how parameter alterations can affect system performance, thereby guiding the optimization of designs to meet stringent engineering criteria with minimal resource utilization. Moreover, the method extends its utility by providing a mechanism to calculate derivatives of critical quantities in relation to one or more independent variables, thus enhancing the accuracy with which sensitivities are understood and applied in practical fluid dynamics settings. This dual capability makes the adjoint method a cornerstone for both theoretical exploration and practical

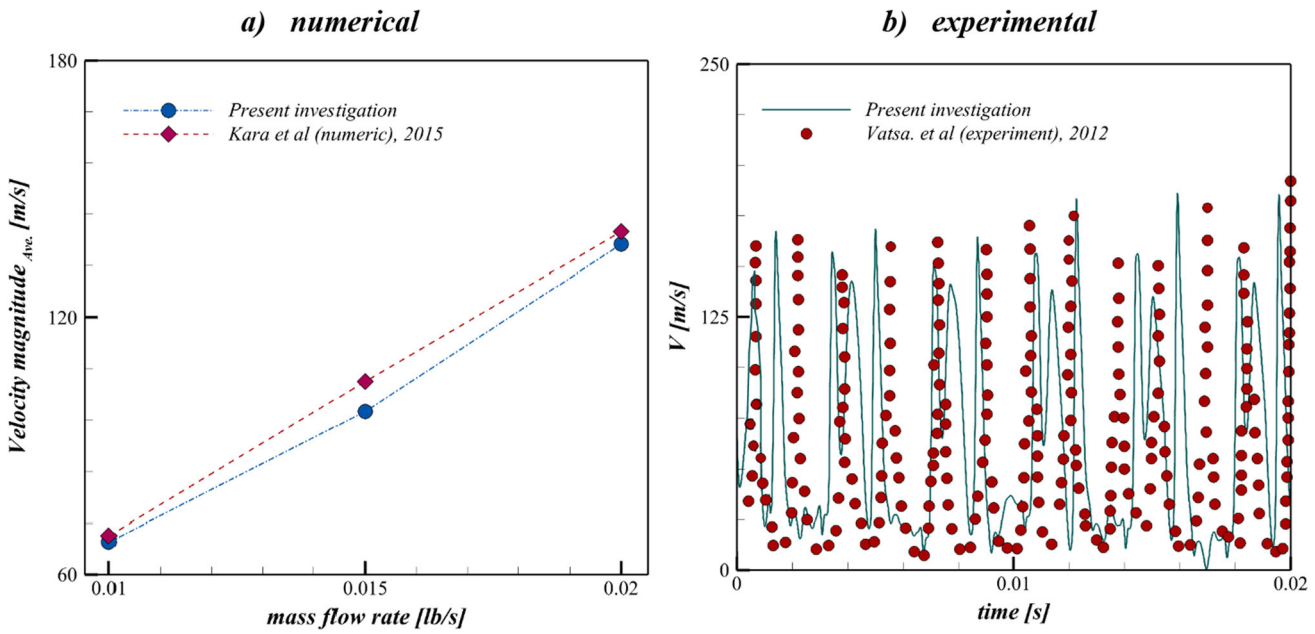

Fig. 6 Validation of the time variation of **a** velocity magnitude at various mass flow rate, **b** velocity time-series at sampling point (6, 0) and mass flow rate = 0.015, to demonstrate consistency between the numerical and experimental results and present data

application in the design and optimization of fluid dynamic systems. The Navier–Stokes equations;

$$\frac{\partial \rho}{\partial t} + \nabla.\left(\rho \vec{U}\right) = 0 \tag{2}$$

$$\frac{\partial\left(\rho \vec{U}\right)}{\partial t} + \nabla.\left(\rho \vec{U} \otimes \vec{U}\right) = -\nabla p + \nabla.\left(\mu \nabla \vec{U}\right) \tag{3}$$

$$\frac{\partial \rho k}{\partial t} + \nabla.\left(\rho \vec{U} k\right) = \nabla.\left[\left(\mu + \frac{\mu_t}{\sigma_k}\right)\nabla k\right] + p_k - \frac{\rho\sqrt{k^3}}{L_{DES}} \tag{4}$$

$$\begin{aligned}\frac{\partial \rho \omega}{\partial t} + \nabla.\left(\rho \vec{U} \omega\right) = \nabla.\left[\left(\mu + \frac{\mu_t}{\sigma_\omega}\right)\nabla \omega\right] \\ + 2\left(1 - F_1\right)\rho \frac{\nabla k.\nabla \omega}{\sigma_{\omega_2}\omega} \\ + \alpha \frac{\rho}{\mu_t} P_k - \beta \rho \omega^2\end{aligned} \tag{5}$$

can be rewritten in a semi-discrete form as follows;

$$\frac{dw_{ijk}}{\partial t} + R_{ijk}(w) = 0 \tag{6}$$

where $w = (\rho, \rho U, \rho k, \rho w)^T$ $w = (\rho, \rho U, \rho k, \rho w)^T$ is the vector of primary variables, and R represents the remaining total. To model changes applied to the solution, it is assumed that a source term is added to the continuity equations and momentum as follows:

$$\tilde{R} = R + S \tag{7}$$

These terms can be fully defined or defined only for mass. An additional vector sign is used to distinguish sensitivity terms from the effect of body forces on the fluid. It is noteworthy that this method is general and can be used to model any type of problem. The additional information obtained plays a significant role in improving numerical solutions. Regions with high sensitivity indicate a strong influence on the solution, and modifications can be considered in those areas.

The adjoint method is divided into continuous and discrete categories. The continuous adjoint method relies on the mathematical features of partial differential equations that define the physical problem. Although it is straightforward to use, it is not applicable to problems with complex boundary conditions and wall functions. On the other hand, the discrete adjoint method is based on the discretized form of these equations. In this approach, the adjoint method is closely connected to the flow solver, and valuable sensitivity information is obtained. This method can also be used in problems involving boundary conditions and complex physics. In this study, the discrete adjoint method was employed, and the adjoint equations are obtained based on the Giles method [51], as follows:

$$\left[\frac{\partial R}{\partial w}\right]^T \psi = \frac{\partial F}{\partial w} \tag{8}$$

where $F = F(w, S)$ represents the monitoring function, w is the vector of fluid-related variables such as pressure and

velocities (referred to as state variables), and S is the control variables obtained from the flow solution. ψ represents the adjoint variable, and R denotes convergence in the fluid equations, defined as follows:

$$R\left(w^0, w^1, \ldots, w^{M-1}; S\right) = 0 \tag{9}$$

M represents the number of cells in the problem. In fact, the values of F, R, and their derivatives are obtained after solving the flow equations. Based on the adjoint equations, the adjoint variables become readable. The sensitivity of the monitoring function to control variables is also derived from the adjoint method as shown below:

$$g = \frac{dF}{dS} = \frac{\partial F}{\partial S} - \psi^T \left[\frac{\partial \tilde{R}}{\partial S}\right] \tag{10}$$

In contrast to the adjoint system in Eq. (8), the effect of design variables in the above equation is defined as a gradient, although vectors and matrices are defined as partial derivatives. Similar to the calculation process of the existing terms in Eq. (8), the computational process of dF/dS and dR/dS is obtained using the method of mean of automatic differentiation [52].

2.8 Numerical Implementation

In this numerical implementation, the discrete adjoint method was integrated into the existing CFD solver framework as follows:

- *Adjoint Solver Integration*: The adjoint solver was developed to interface seamlessly with the forward flow solver. This integration ensures that the adjoint equations are constructed using the same discretization scheme and mesh configuration as the forward problem, maintaining consistency and accuracy.
- *Boundary Conditions*: Appropriate boundary conditions for the adjoint variables were applied, mirroring the physical boundary conditions of the forward problem. For instance, at inlet and outlet boundaries, adjoint variables were set to zero, while at walls, symmetry conditions were enforced.
- *Iterative Solution Process*: The forward and adjoint problems were solved iteratively. First, the steady-state flow solution w_0 is obtained by solving the Navier–Stokes equations. Subsequently, the adjoint equations are solved using the obtained flow field to determine ψ. This process is repeated until convergence is achieved for both the forward and adjoint solutions. Additionally, the adjoint-based gradients were compared with finite difference approximations to verify their correctness.

2.9 Sensitivity Analysis Procedure

The sensitivity analysis was conducted following these steps:

- *Objective Function Definition*: The objective function F was defined as the pressure drop across the fluidic oscillator, a critical performance metric influencing overall efficiency.
- *Design Parameter Identification*: Key design parameters, including surface curvature and boundary condition variations, were identified for sensitivity evaluation.
- *Adjoint Equation Solving*: For each design parameter, the adjoint equations were solved to obtain the corresponding adjoint variables ψ.
- *Gradient Computation*: Using the adjoint variables, the gradient dF/dS was computed, indicating the sensitivity of the pressure drop to each design parameter. The sensitivity gradients guided the optimization process, enabling targeted modifications to design parameters that would most effectively reduce pressure drop and enhance performance.

3 Result and Discussion

In the present study, enhancing the performance of a sweeping jet was the main aimed, with a particular focus on increasing the outlet jet frequency, a key distinguishing factor in superior sweeping jet designs. Recognizing the crucial role of drop pressure in shaping the outlet jet characteristics, sensitivity analysis was conducted to pinpoint which components of the sweeping jet had the most significant impact on the pressure drop.

The applied methodology involved systematically assessing the sensitivity of various parts of the sweeping jet to changes in shape, with a specific emphasis on Coanda surfaces and feedback channels. The outcomes of this analysis were visually represented in Fig. 7a that compared the shape sensitivity of all sweeping jet walls and included x and y shape sensitivity vectors (See Fig. 7a), offering a comprehensive view of how different regions of the sweeping jet influenced drop pressure.

In scrutinizing the shape sensitivity on Coanda surfaces and feedback channels, it is imperative to draw upon Bernoulli's equation and the principles of fluid continuity. The results of the present work suggest that modifications at the trailing edge (Refer to Fig. 2 for details) of the Coanda surfaces substantially affect the velocity and pressure of the jet stream due to changes in the cross-sectional flow area. This area directly influences the momentum balance, hence altering the oscillation frequency of the sweeping jet, as predicted by the momentum conservation equations. The core

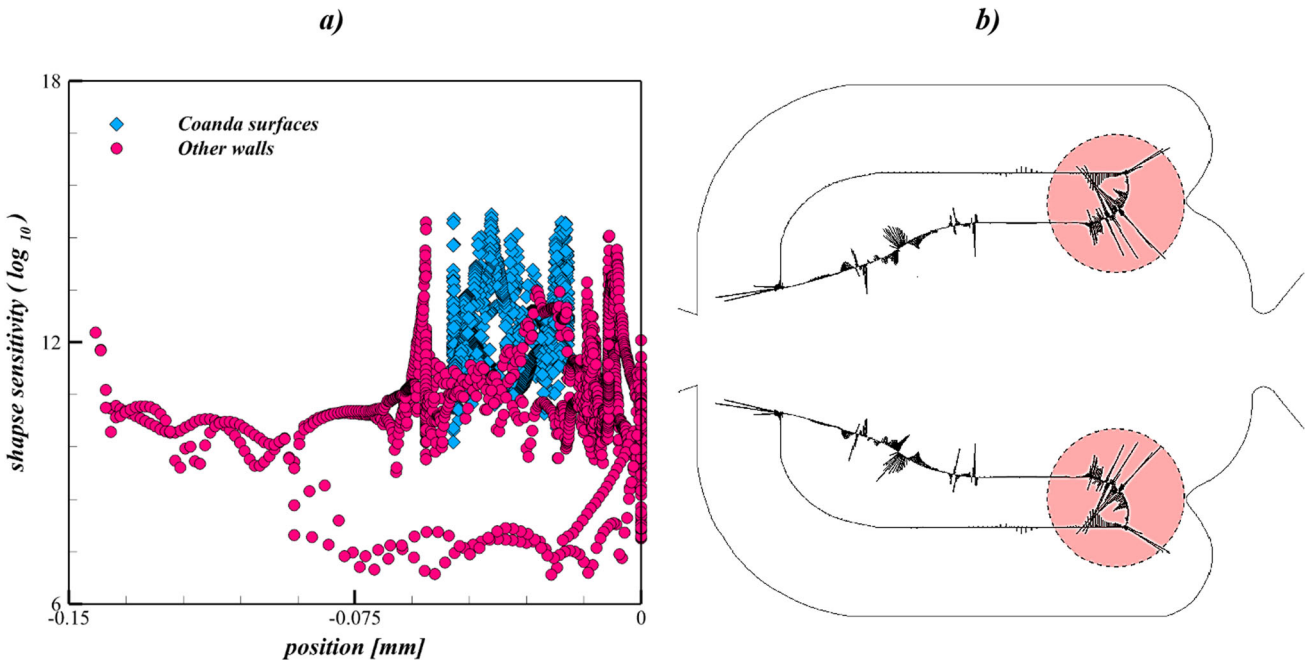

Fig. 7 Sensitivity analysis of pressure drop on the original SWJ, **a** shape sensitivity distribution, highlighting regions most influencing pressure drop, **b** vector plot indicating flow sensitivity near the Coanda surface, where geometric refinements may reduce losse

of the present sensitivity analysis lies in the adjoint method, a powerful technique widely recognized for its efficiency in calculating gradients in high-dimensional spaces. In fluid dynamics, this technique determines the sensitivity of a certain output (in this case, the pressure drop and jet frequency) to input parameters (the shape of Coanda surfaces). Figure 7a illustrates of the shape sensitivity profiles was derived from adjoint solutions, which efficiently computed the gradients of the pressure drop. This gradient information, visually summarized by the sensitivity vectors in Fig. 7a, directs the investigation toward the most impactful geometric modifications for optimizing the oscillator's performance.

These vectors convey the rate of change of pressure with respect to spatial alterations which will yield the highest performance gain. The adjoint method extends beyond a mere numerical tool; it reflects the underpinning physical phenomena of fluid–structure interactions. By understanding the adjoint variables as 'shadow' fields that communicate how perturbations in the flow field propagate backward in time, can gain insight into the causative relationship between shape modifications and flow behavior. To augment the clarification, Fig. 8a highlights the interdependent relationship between the surface curvature and pressure distribution, a relationship dictated by the Coanda effect and substantiated by the NS equations for incompressible flow. The oscillatory behavior of the sweeping jet is also a manifestation of the Strouhal number's relevance in fluidic oscillator design, correlating with the frequency of vortex shedding from the trailing edge, as shown by the modifications. (Refer to Fig. 2 for details.)

3.1 Commencement Stages of Jet Formation in the Modified Oscillators

3.1.1 Dynamics of Jet Formation

The initial stages of jet formation in modified oscillators are characterized by complex vortex dynamics within the oscillator chambers. As illustrated in Fig. 8a–f, two primary vortices emerge, driving the jet's trajectory through the inlet throats and its interaction with modified Coanda surfaces, which in turn dictate the observed oscillatory behavior. These vortices, as shown in Fig. 8a′, c′, d′, f′, g′ and i′, play a pivotal role in defining the jet's subsequent path, mainly through their pronounced interactions with the jet's shear layer. Such interactions are crucial for momentum exchange and vorticity enhancement, which are foundational to the oscillatory movements noted. Vortex dynamics are integral, where the rotation of fluid elements, adhering to the conservation of angular momentum, profoundly influences the stability and direction of the jet. This dynamic is evident as the jet navigates through geometric modifications, disrupting its symmetrical flow and prompting the asymmetric expansion and contraction of the vortices. This asymmetry is key to amplifying oscillation amplitude, as depicted in the gradual intensification observed in subsequent figures Fig. 8a′, c′, d′, f′, g′ and i′. The nuanced interplay between these vortices

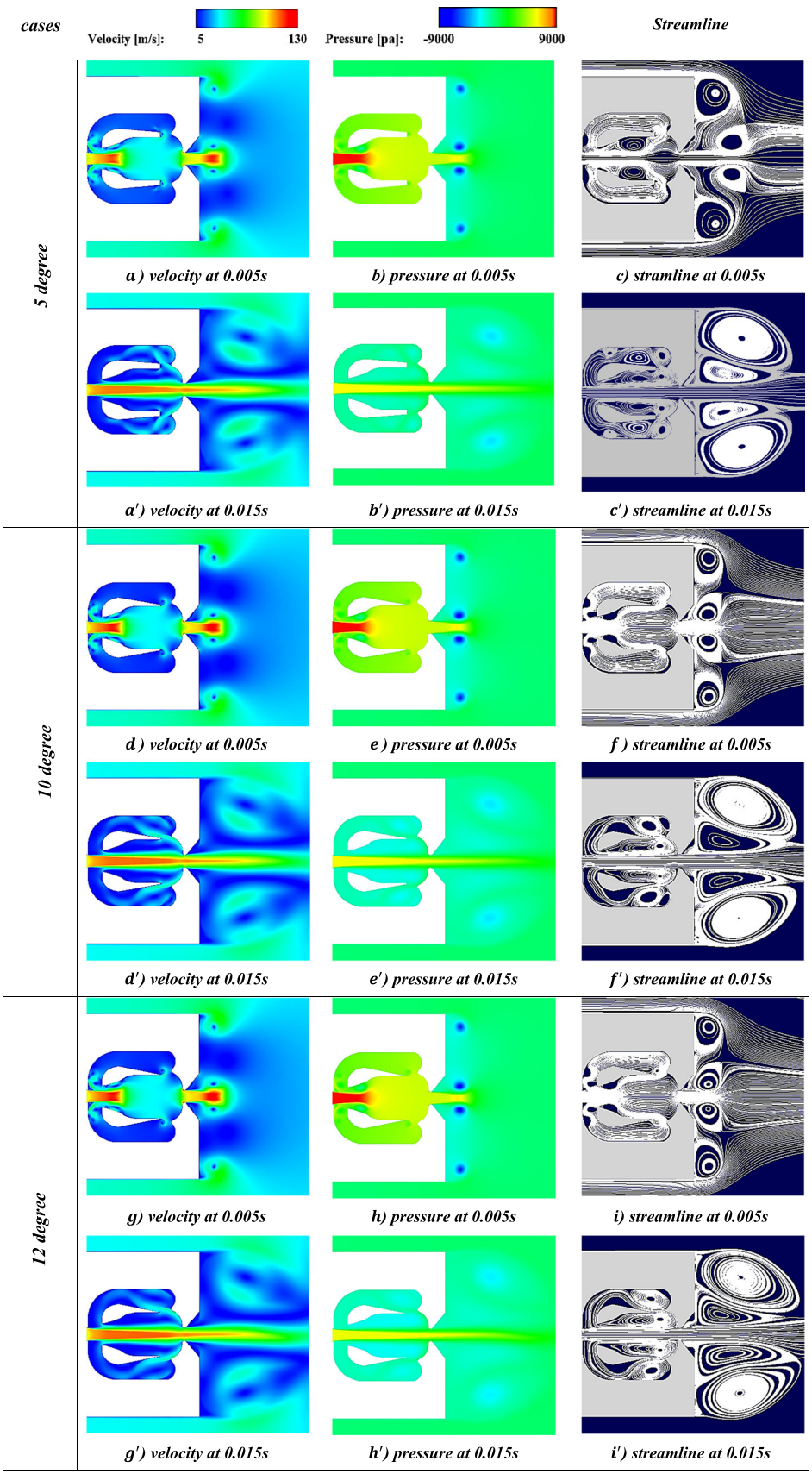

Fig. 8 Contours of velocity and pressure, along with streamlines, at early simulation times. These snapshots show the onset of jet oscillation and emerging vortices for 5°, 10°, 12°

and the jet's shear layer underscores the significant role of internal chamber geometry in jet behavior modulation.

The pressure contours (Fig. 8b, b′, e, e′, h and h′) underscore a gradient conducive to the operational mechanism of the fluidic oscillator. The lowered pressure within the primary chamber enables the inflow of feedback air, crucial for initiating the jet's oscillation. This reduction in pressure, especially within the vortex cores of the primary chamber, triggers extensive airflow dynamics vital for the jet's oscillatory motion. Such pressure dynamics elucidate Bernoulli's principle, where the decrease in pressure correlates with an increase in velocity, fostering a critical inflow of air that sustains the oscillator's functionality. Differential pressures across the chambers, influenced by throat dimensions, profoundly impact the internal flow dynamics. Additionally, the pronounced Coanda effect, which describes the fluid jet's propensity to adhere to convex surfaces, plays a pivotal role in the device's performance. This effect, manipulated through geometric alterations of the oscillator, illustrates how fluids tend to follow curved paths, crucial for directing the jet within the oscillator and ensuring stable oscillatory motion. The distinct pressure characteristics between the primary and secondary chambers, influenced by variations in throat dimensions, highlight the Coanda effect's instrumental role in enhancing the oscillator's efficiency to produce desired oscillatory patterns.

3.1.2 Interpreting the Modified Oscillators Mechanism

The progression from symmetrical to asymmetrical vortex growth, as detailed in Fig. 8a'–i', indicates that the fluidic oscillator is highly responsive to minute geometric modifications. These modifications influence the flow separation points, significantly impacting the jet's oscillation frequency and amplitude. The interaction of the emerging vortices with the jet's shear layer not only disrupts the flow pattern but also amplifies the exchange processes that govern the oscillation dynamics. The study employs the adjoint method to systematically optimize the oscillator geometry for specific flow characteristics, enhancing the design for varied applications such as flow control and mixing processes. The energy within the system, manipulated through geometric adjustments to the Coanda surface, facilitates the necessary modifications in the jet's momentum and oscillation characteristics. These adjustments prove critical in the enhanced functionality of the oscillators, tailoring them to meet specific operational criteria.

Indeed, specifically when adjusted to 12°, the oscillator's modifications trigger the initiation of oscillation. This onset is primarily driven by the deliberate generation and control of vortices within the primary chamber, as clearly demonstrated in the last frames of Fig. 8. Charged by the inflow of the jet and molded by the chamber's geometry, these vortices lead to substantial, yet intricately organized internal turbulence. This organization is not coincidental but a direct consequence of the geometric constraints of the oscillator's design, which not only directs the jet's path but also catalyzes its oscillation.

Moreover, the dynamics within the primary chamber at this specific adjustment result in a pressure drop, which is crucial in activating a feedback mechanism essential for sustained oscillation. This mechanism is underpinned by fluid mechanics principles, whereby the pressure differential between the primary and secondary chambers propels air back into the primary chamber. This action reinforces the jet's motion and sustains the oscillatory cycle. Therefore, the amplitude and frequency of the jet's oscillation, significantly influenced by the asymmetric growth and contraction of the vortices, are intricately linked to the fluid's inertial and viscous forces. These forces are meticulously calculated and optimized through fluid dynamics simulations to fine-tune the oscillation characteristics needed. Through these interactions, the geometric modifications of the oscillator provide a tunable mechanism to adapt its performance for specific application requirements (Figs. 9, 10, 11).

3.2 Comparison Between the Modified and Original Oscillators

This section involves a comparison of the operational performance of the modified and original oscillators once harmonic oscillations have been attained. Figure 9 illustrates the asymmetric growth and contraction of the two pairs of vortices at different time intervals, giving rise to a sinusoidal pattern within the oscillator jet, particularly evident in cases 10° and 12°. This figure reveals that within the modified oscillator, the jet primarily interacts with the two pairs of vortices rather than the chamber walls, resulting in reduced jet momentum depreciation and lower pressure losses. Additionally, in the modified cases, increasing the throat at the trailing edge presents new challenges for the vortices. To elaborate two critical interval was selected (t_2 and t_6 See Fig. 12), as indicated by the red rectangle in the original case, the vortices are initially separated, leading to lower-frequency behavior.

The vortex dynamics within the fluidic oscillator are significantly influenced by the Coanda surface modifications. At the first critical time interval, t_2, the streamlines in the original configuration exhibit clear separation, resulting in lower interaction frequencies. However, as the modifications are introduced, the dynamics evolve noticeably. At a 5-degree modification, the streamlines suggest a nascent interaction between the vortices, but it is at the 10- and 12-degree modifications that the vortices' interaction becomes markedly pronounced. The 10-degree case offers a transitional behavior, where the vortices exhibit a growing tendency to merge. This trend reaches its top in the 12-degree case, showcasing

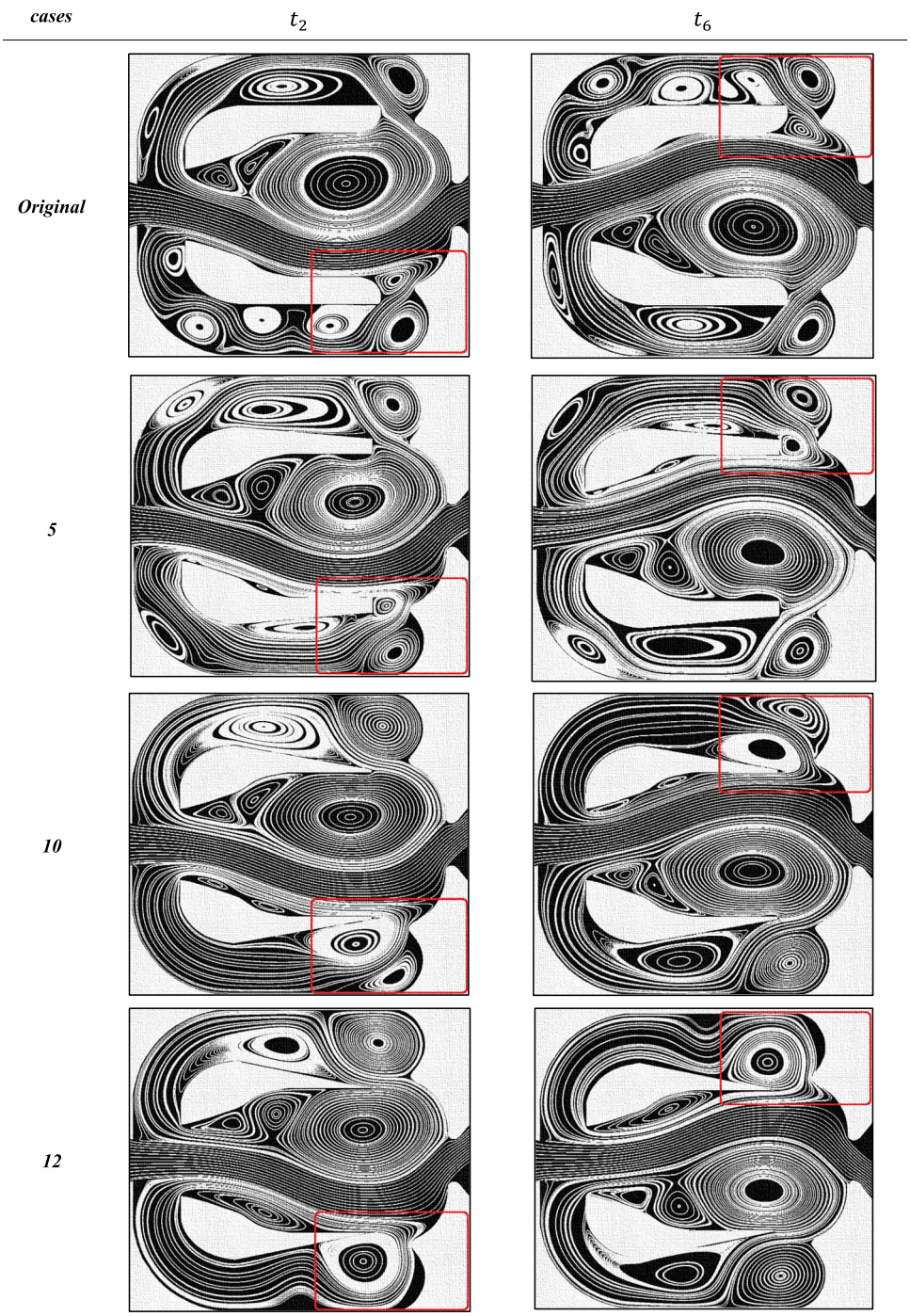

Fig. 9 Streamlines inside the oscillator at 2 equal intervals of a time period, illustrating how the jet switches sides and how vortices evolve once harmonic oscillations are established for 5°, 10°, 12°

a significant combination of the vortex cores, indicative of an intensified fluid dynamic interaction.

The 12-degree modification's superior performance can be attributed to several fluid dynamic principles. First, the flow separation is delayed, which, according to boundary layer theory, is indicative of a stronger attachment of the flow to the modified Coanda surface. This phenomenon is rooted in the adverse pressure gradient's modulation, which is a direct consequence of the geometric alterations. Second, the observed vortex merger is congruent with the Kelvin–Helmholtz instability principle, where the increased angle enhances the interaction between the vortices, leading to a higher combination rate. This interaction fosters a stronger and more coherent jet oscillation, as predicted by the Biot-Savart law, which underscores the mutual induction of vortical structures.

Furthermore, the pressure field alterations due to the surface modifications have direct implications on the jet's

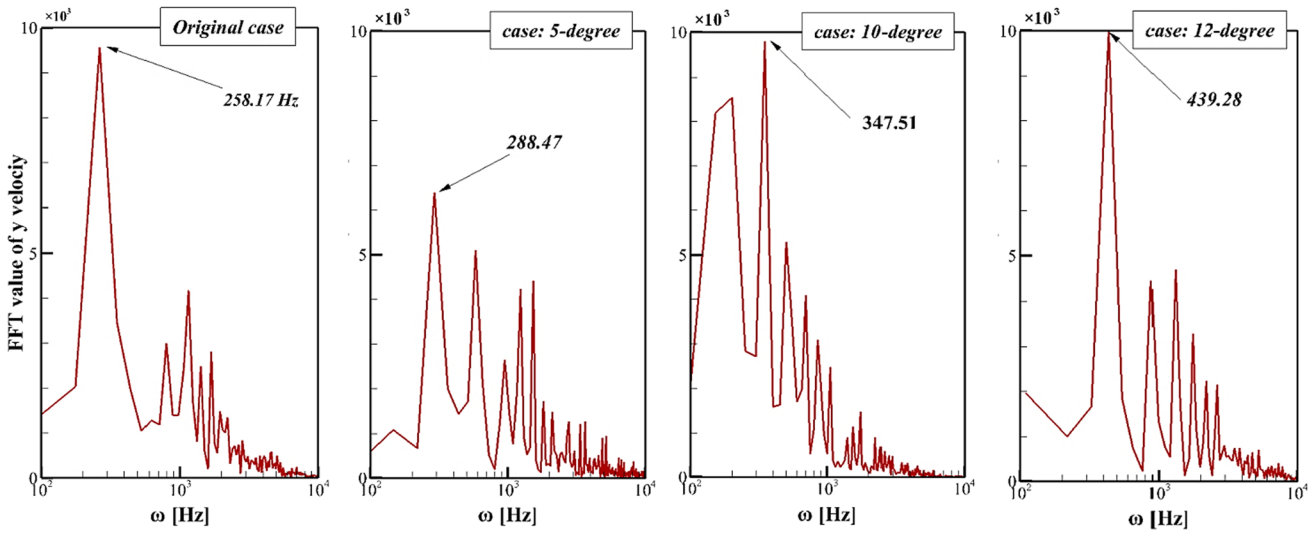

Fig. 10 Frequency spectra of the outlet velocity signal for the baseline and modified Coanda surface configurations, highlighting shifts in oscillation frequency

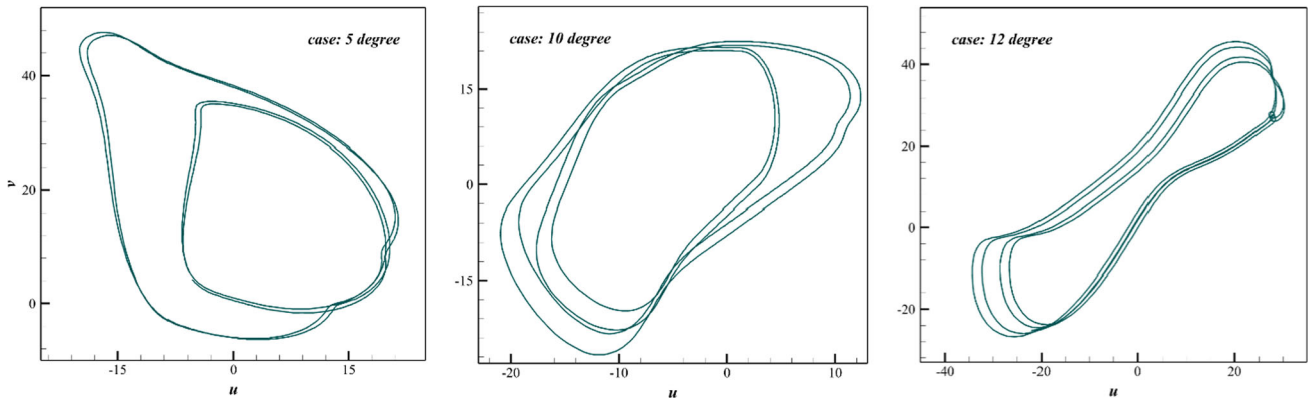

Fig. 11 View of phase portraits orbits for modified models including 5°, 10° and 12°, each orbit indicates how the oscillatory behavior changes with Coanda surface angles, illustrating differences in amplitude, frequency, and overall stability

momentum. The reduced pressure losses in the 12-degree case suggest a more efficient momentum transfer, translating to higher oscillation frequencies and improved resonance characteristics. This improvement aligns with Bernoulli's principle, where the velocity increase within the oscillator's throat leads to a corresponding drop in static pressure, enhancing the oscillator's efficiency. This comparative analysis confirms that the 12-degree modification significantly optimizes the fluidic oscillator's performance. The increased frequency and resonance characteristics have potential applications in enhancing mixing efficiency in various industrial processes, fine-tuning acoustic control in noise reduction technologies and improve the process of flow control and heat transfer.

3.3 Frequency Analysis

3.3.1 Fast Fourier Transform

The study of oscillatory systems is profoundly augmented by the analysis of their frequency components. These analyses elucidate the dynamic nature of such systems and are indispensable for the optimization of their performance [53]. In the realm of fluid dynamics, particularly within the context of fluidic oscillators, the comprehension of outlet frequencies is a focal point of interest. The current investigation pivots on the modulation of these frequencies via alterations in the feedback channel of oscillators, using fast Fourier transform (FFT) as the analytical tool of choice. An innovative approach was employed where a diffuser was integrated into the feedback channel, intended to perturb the flow characteristics and consequently, the outlet frequency (See Fig. 2).

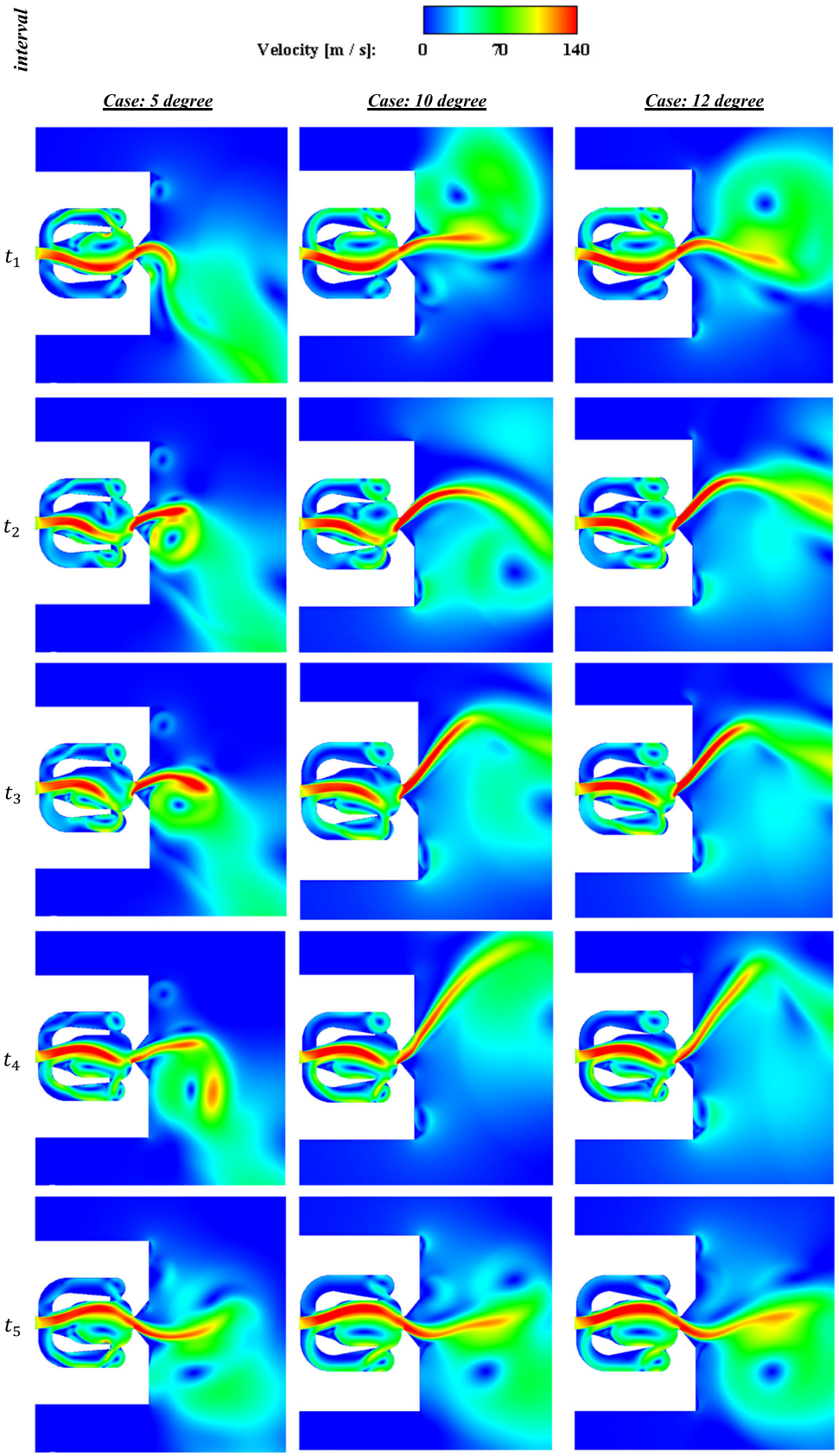

Fig. 12 Contours of velocity at eight equal intervals of a time period in one full cycle, each column corresponds to a Coanda surface modification angle (5°, 10°, or 12°), highlighting differences in jet sweeping and flow structure

Fig. 12 continued

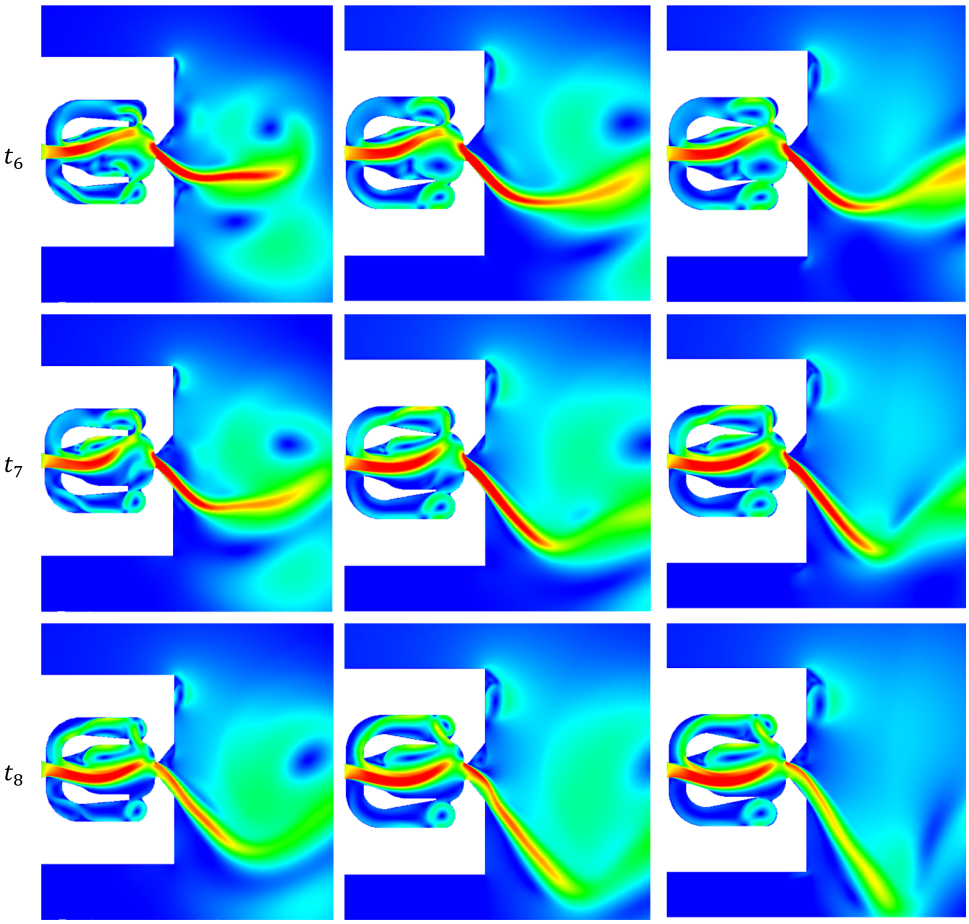

As delineated in Fig. 10, variations in the throat dimensions, specifically an increase by 35, 50, and 60% in the trailing edge throat compared to the inlet, induced significant escalations in the outlet frequency to 288.47, 347.51, and 439.28 Hz, respectively. These alterations are not merely quantitative but also qualitative, as they underscore the critical influence of the feedback channel's design on the fluidic oscillator's functionality. The fluidic oscillator's narrative is profoundly shaped by its geometry. The unmodified baseline FFT peak at 258.17 Hz evolves remarkably with progressive geometric adjustments, ascending to peaks of 288.47, 347.51, and finally, 439.28 Hz. These modifications unravel the intricate relationship between the Coanda surface angles and the dynamic flow patterns, echoing the principle of minimal geometric changes yielding significant fluid dynamic consequences.

The enhanced peak at 439.28 Hz in the 12-degree case unveils an intriguing shift in the fluid dynamic behavior. This peak is not an isolated metric but an indicator of the reconfigured pressure distribution and flow separation points, intrinsic to the vortex shedding phenomenon. Here, the increased frequency and energy of the oscillations align with the adjusted geometry, affirming the intimate connection between structure and performance. Additionally, the analysis surfaces a correlation between the trailing edge throat expansion and the mass flow rate. The expanded throat signifies a higher volume of flow, dovetailing with an intensified energy transfer apparent in the escalated oscillation frequencies. In the original FFT diagram, the dominant peak at 258.17 Hz represents the fundamental frequency of the oscillator. This peak is the primary harmonic and is a direct consequence of the oscillator's design parameters under unmodified conditions. Subharmonic peaks, which are lower frequency components that appear as smaller spikes in the FFT, reflect the system's inherent flow instabilities and resonances at submultiples of the fundamental frequency.

Upon a 5-degree adjustment, the FFT peak shifts to 288.47 Hz, a higher frequency suggesting a stiffer system response due to the altered geometry. The harmonics in this case, while still clearly defined, show a shift in their distribution, indicating a change in the system's resonant frequencies. This is harmonizing with a modified flow path that accelerates the fluid, altering the characteristic frequencies of the flow-induced vibrations. Further modifications to 10 and 12 degrees result in peaks at 347.51 and 439.28 Hz, respectively.

The 10-degree case shows a broader spread of harmonic content, which can be linked to an increased complexity in flow behavior, potentially due to greater vortex strength and interaction. In the 10-degree case, the subharmonic suggests that the flow within the oscillator is experiencing a complex interaction between the oscillatory motion imposed by the feedback loop and the natural vortex shedding frequency. The feedback loop's frequency may not be harmonically related to the vortex shedding, thus introducing energy into the system at a subharmonic frequency.

From the fluid dynamics perspective, when such subharmonics are observed, it is critical to consider their potential effects on the performance and stability of the fluidic oscillator. Subharmonics can lead to unpredictable behaviors, which may be detrimental or beneficial, depending on the intended application of the oscillator. Understanding and controlling these subharmonics are key aspects of designing fluidic systems for precise applications. The 12-degree case, exhibiting the highest peak, is indicative of the most significant alteration in flow dynamics. This case may demonstrate a higher harmonic generation due to stronger, more coherent vortex shedding as the flow reattaches at more pronounced angles on the Coanda surface.

Comparing these cases, one observes a trend of increasing harmonic frequency with increased feedback channel modification. The subharmonic content also becomes more complex with modification, which can be associated with nonlinear interactions between the vortices and the oscillator walls. Such interactions are known to influence the efficiency and stability of the fluidic oscillator's output. The subharmonic content, particularly in the 10-degree and 12-degree cases, suggests the presence of bifurcations in flow behavior, possibly transitioning to a chaotic regime. This is consistent with fluid dynamics, where increasing the system's Reynolds number, either by changing geometry or flow conditions, can push the flow toward a chaotic state, characterized by a rich harmonic and subharmonic spectrum.

3.3.2 Phase Portraits Circuits

Figure 11 illustrates phase portrait circuits for modified models at 5°, 10°, and 12°, essential for understanding the impact of Coanda surface modifications on vortex dynamics and the operational efficiency of fluidic oscillators. The phase portrait for the 5-degree modification shows a notable deviation from the original configuration, indicative of irregular vortex strength and interaction. This irregularity mirrors the behavior of an unmodified system, characterized by low efficiency and a pronounced susceptibility to adjacent vortex influences. Despite observable peak velocities associated with the external jet flow's upward trajectory, the low outlet frequency highlights inconsistencies in vortex formation. Minor changes at this angle suggest limited improvements in flow dynamics due to minimal alterations in boundary layer characteristics. Consequently, this modification does not significantly enhance the oscillator's performance, as it lacks the pronounced streamline curvature necessary for effective Coanda attachment.

In contrast, the 10-degree and 12-degree modifications exhibit enhanced symmetry in their orbits, indicating uniform vortex formation and a resilient core that withstands external disturbances. These modifications achieve a more coherent and repeatable vortex pattern, signifying controlled jet deflection and harmonic oscillation. The phase portraits for these angles demonstrate the successful utilization of the Coanda effect, improving momentum exchange. Specifically, the 10-degree modification shows a complex orbit pattern with closed loops, indicating strong, sustained jet attachment. This increased curvature enhances the surface's ability to guide the fluid, using viscous forces to maintain jet attachment and induce stable oscillations. At 12°, the phase portrait reveals a highly consistent and repetitive pattern, suggesting an optimal balance between jet attachment and detachment points. This increased angle creates a conducive environment for prolonging the jet stream's effective action, enhancing the oscillator's performance with a more defined oscillation pattern.

3.4 Dynamic Characteristics

Across all cases, Fig. 12 presents the dynamic nature of the jet oscillations and the influence of throat geometry on fluid behavior. At each interval, can be observed the following:

- t_1 to t_3: The establishment of baseline flow patterns and initial vortex formation. This phase is critical in determining the subsequent behavior of the jet oscillations.
- t_4 to t_6: The growth and interaction of vortical structures with the jet and surrounding fluid. This stage is indicative of the oscillation's strength and sustainability.
- t_7 to t_8: The fully developed oscillatory flow, where the consequences of the geometric modifications are fully realized in the form of enhanced or suppressed oscillations.

The modified oscillators, which involve enlarging the throat at the trailing edge, are shown to induce considerable fluctuations in the jet stream. This is primarily due to the disruption of vortex symmetry within the oscillator chambers, which is accentuated by the non-uniform expansion and contraction of vortex pairs. Such modifications lead to amplified jet oscillations, with the maximum amplitude being contingent on the dimensions of the trailing-edge throat. This relationship is supported by frequency analysis (See Fig. 10) indicating that similar dimensions of the throat at both the leading and trailing edges (as in the original design) diminish

the oscillator's efficiency due to reduced vortex strength in the primary chamber.

The 5-degree case exhibits a significant jet adherence to the Coanda surface, a phenomenon consistent with the Coanda effect. At initial time intervals (t_1 and t_2), the flow is attached closely to the curved surface due to the narrow trailing edge, which limits the development of large-scale vortical structures and confines the jet, resulting in a subdued oscillatory behavior. As time progresses (t_3 to t_8), the jet maintains its close proximity to the Coanda surface, indicating that the confined geometry restricts the lateral expansion and the energy available for inducing strong oscillations. With the 10-degree modification, there is a noticeable increase in the low-pressure zone's breadth, especially observable from t_4 to t_8. This change facilitates a more pronounced entrainment of ambient fluid into the jet stream, enhancing mixing and vortex formation. The resulting flow structure is indicative of an increased oscillation amplitude, as can be seen from the broader jet spread and the more pronounced vortical structures detaching from the Coanda surface. In the 12-degree scenario, the expanded trailing edge throat dimension is visually impactful in the later time intervals (t_6 to t_8), where the asymmetry in the vortical structures becomes more pronounced, correlating with a significant amplification in oscillation amplitude. The large vortices that form and shed in this configuration suggest that the oscillator is experiencing vigorous mixing and energy transfer from the flow to the oscillations, resulting in a substantial deflection of the jet.

While the jet oscillates, as it nears the bottom wall of the primary chamber (as shown in Fig. 12), the shear layer tends to continue its path and exits the chamber due to the narrowing of the trailing edges of the Coanda surface (as observed in Fig. 12 for cases at 10° and 12°). As illustrated in Fig. 12 for the 5-degree case, the thick trailing edge of the Coanda surface, combined with the Coanda effect, causes the flow to adhere to the surface and quickly enter the feedback channel, resulting in incomplete development of the oscillator. This significantly impacts the jet oscillation, limiting its amplitude compared to other cases, as clearly seen in Fig. 12. This alteration in flow patterns also affects the pressure gradient, leading to greater disparities as the throat dimension increases at the trailing edge, (See Fig. 13 for cases t_2 and t_3). This increased disparity in pressure gradient contributes to a more effective oscillation, a phenomenon supported by previous research findings [44].

3.4.1 Enhanced Shear Layer and Vortex Intensification

In the modified fluidic oscillators, the pressure differential between the primary chamber and the interior of the bottom feedback channel plays a crucial dual role. Initially, it creates a spatial separation between the jet and the trailing edge of the feedback channel. This separation allows the feedback flow to enter the primary chamber, enhancing fluid mixing and pressure modulation. Secondly, this pressure differential facilitates the formation of a substantial vortex between the jet and the surface of the chamber. As observed in Fig. 12, cases t_2 through t_4, these trapped vortices, with increasingly strong cores due to the enlargement of the trailing edge dimensions, exert a significant upward force on the jet.

The strengthened vortex near the bottom of the primary chamber, as depicted in Fig. 12, case t_3, swiftly redirects the jet away from the bottom wall toward the central region of the chamber. This redirection, as detailed in the analysis, contributes to an intensified shear layer at the core of the jet, thereby amplifying the vortex strength on the lower side of the primary chamber. As the jet ascends and attaches to the upper wall of the secondary chamber, the outward flow from the oscillators deflects downward, leading to a widened upper feedback channel, and subsequently enhanced upper feedback flow into the primary chamber (Fig. 12, cases t_5 through t_7).

The cyclic behavior of the jet as it moves away from the upper wall manifests a growing vortex in the upper section of the primary chamber, eventually expanding to cover both the upper regions of the primary and secondary chambers (Fig. 12, cases t_7 and t_8). This expansion results in a notable pressure differential, depicted through the contrasting red and green regions in Fig. 13, case t_7. This process is reiterated continuously, with similar phenomena observable at critical Reynolds numbers, suggesting the importance of this dynamic in fluid control and oscillator efficiency. When analyzing the jet's performance beyond the confines of the oscillators, it is evident that the modified oscillators (12-degree case) produce a jet with longer persistence and superior momentum as it travels away from the outlet. This is in stark contrast to the original oscillator designs, where the jet tends to adhere closely to the Coanda surface with a thicker trailing edge. Such adherence in the 5-degree case prevents full jet development and results in a noticeable loss of momentum as the jet progresses away from the outlet nozzle (Fig. 12, case t_1). In contrast, the 12-degree modification showcases a faster detachment and more effective expansion, corroborated by higher velocities observed at extended distances from the outlet, which aligns with the fluid dynamics principles of jet expansion.

Moreover, An FFT analysis of the flow at each modification level provides insight into the frequency domain, indicating how alterations in surface angle influence the jet's temporal behavior. For the 12-degree case, a higher frequency peak suggests a more rapid detachment and reattachment cycle, reflecting a more pronounced oscillation.

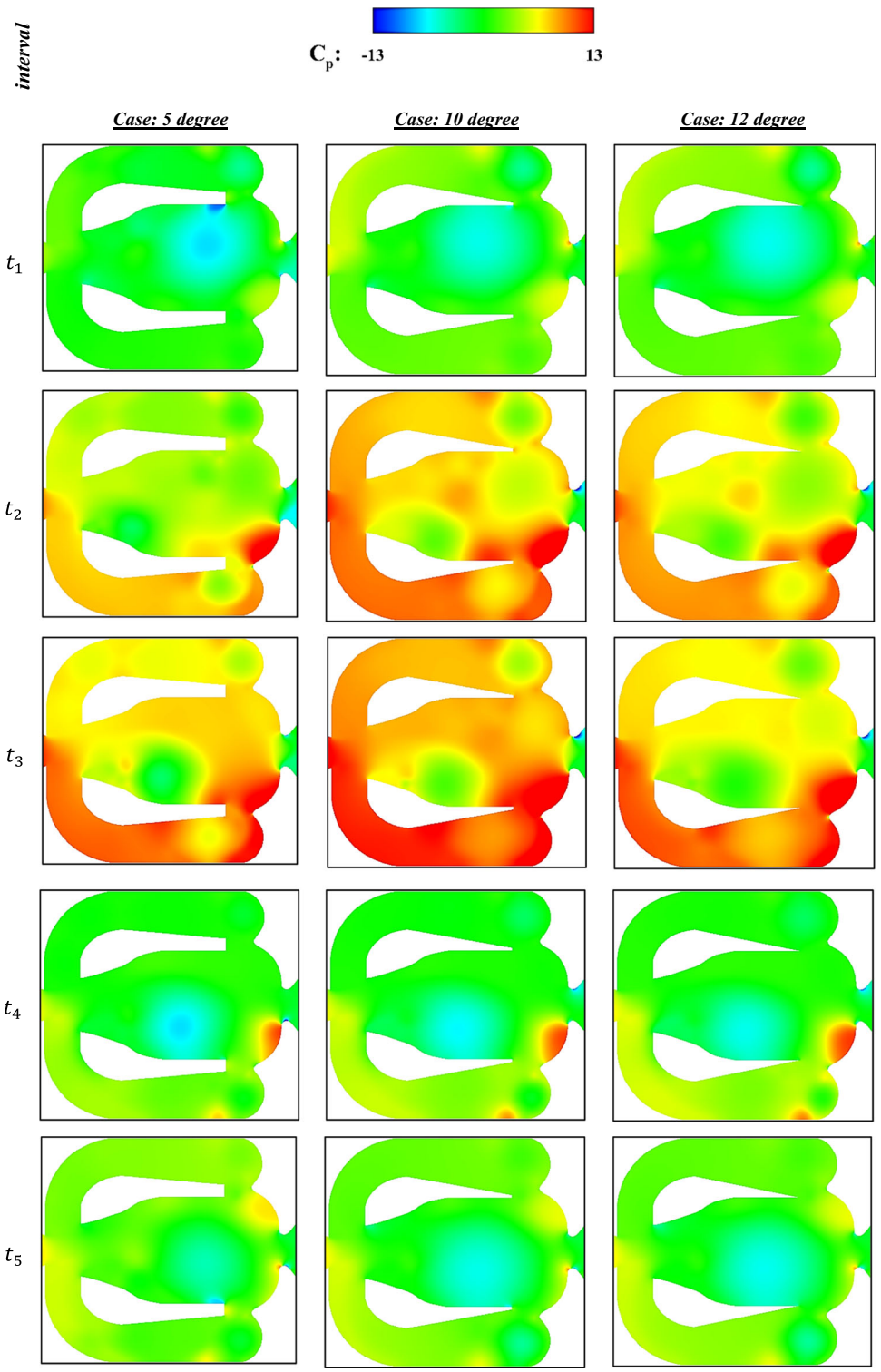

Fig. 13 Pressure coefficient fields at eight equal intervals of a time period in one full cycle, each column corresponds to a Coanda surface modification angle (5°, 10°, or 12°), highlighting the temporal evolution of pressure gradients that drive and sustain jet oscillations

Fig. 13 continued

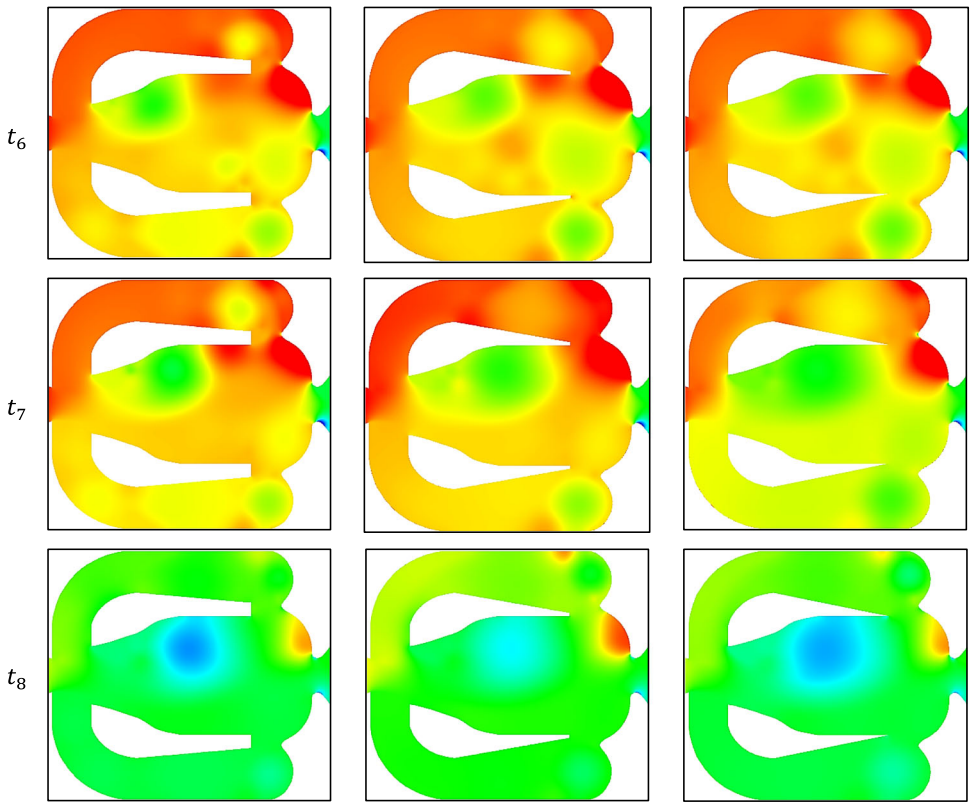

4 Conclusion

This study presents a significant advancement in the design of fluidic oscillators through strategic modifications aimed at reducing internal pressure drops and enhancing outlet jet frequency via optimized feedback channel efficiency. Utilizing a two-dimensional numerical framework based on the URANS equations and the $k-\omega$ Shear Stress Transport turbulence model, the effects of redesigned Coanda surfaces were thoroughly investigated.

The removal of trailing edges on the Coanda surfaces facilitated asymmetrical vortex merging within the primary chambers, effectively initiating and sustaining jet oscillations. This design alteration resulted in an 18% reduction in internal pressure drops and a substantial 70% increase (from 258.17 Hz in the original case to 439.28 Hz in the modified 12-degree case) in oscillation frequency compared to the baseline design. Additionally, the modified oscillators demonstrated a higher frequency-deflection-pressure ratio, indicating enhanced operational efficiency. Comparative analysis revealed that the redesigned oscillators consistently produced continuous jets with lower oscillation amplitudes, thereby minimizing momentum loss and promoting a more streamlined flow toward the outlet. Furthermore, the jets from the modified oscillators exhibited expanded spreading angles, resulting in enhanced mass and momentum fluxes compared to the original design. These improvements are attributed to the optimized feedback channel design, which intensified the oscillatory behavior of the jet stream and stabilized external flow dynamics.

The quantitative enhancements observed, including a 18% decrease in pressure drop and a 70% increase in oscillation frequency, validate the effectiveness of the Coanda surface redesign in promoting more stable and efficient oscillatory behavior. These findings underscore the potential of the modified fluidic oscillators for applications requiring precise flow control and increased fluid dynamic efficiency, such as in aerodynamic flow management, thermal systems, and energy harvesting technologies.

In conclusion, the systematic redesign of the Coanda surfaces, informed by rigorous computational analysis and sensitivity assessments, has substantially enhanced the performance of fluidic oscillators. These advancements not only validate the proposed modifications but also highlight the broader applicability and efficiency improvements achievable through optimized geometric configurations in fluidic systems.

References

1. Kim, S.H.; Kim, H.D.: Quantitative visualization of the three-dimensional flow structures of a sweeping jet. J. Vis. **22**, 437–447 (2019). https://doi.org/10.1007/s12650-018-00546-1

2. Tomac, M.N.: Novel jet impingement atomization by synchronizing the sweeping motion of the fluidic oscillators. J. Vis. **23**, 373–375 (2020). https://doi.org/10.1007/s12650-020-00632-3
3. Gomes, R.; Barbosa, F.V.; Teixeira, J.C.F.: Flow dynamics and heat transfer analysis of a sweeping air jet–an experimental approach. Int. J. Heat Mass Transf. **227**, 125479 (2024). https://doi.org/10.1016/j.ijheatmasstransfer.2024.125479
4. Agricola, L.; Prenter, R.; Lundgreen, R.; Hossain, M.; Ameri, A.; Gregory, J.; Bons, J.: Impinging sweeping jet heat transfer. In: 53rd AIAA/SAE/ASEE Joint Propulsion Conference, American Institute of Aeronautics and Astronautics, Reston, Virginia, (2017). https://doi.org/10.2514/6.2017-4974.
5. Ming, T.; Wang, Z.; Liao, X.; Shi, T.; Tan, G.; Wu, Y.: Unsteady RANS simulation of fluid dynamic and heat transfer in an oblique self-oscillating fluidic oscillator array. Int. J. Heat Mass Transf. **177**, 121515 (2021). https://doi.org/10.1016/j.ijheatmasstransfer.2021.121515
6. Ostermann, F.; Woszidlo, R.; Nayeri, C.; Paschereit, C.O.: Experimental comparison between the flow field of two common fluidic oscillator designs. In: 53rd AIAA Aerospace Sciences Meeting, American Institute of Aeronautics and Astronautics, Reston, Virginia, (2015). https://doi.org/10.2514/6.2015-0781.
7. Yuan, C.; Zhang, H.; Li, X.; Oishi, M.; Oshima, M.; Yao, Q.; Li, F.: Numerical investigation of T-shaped microfluidic oscillator with viscoelastic fluid. Micromachines. **12**, 477 (2021). https://doi.org/10.3390/mi12050477
8. Bergadà, J.M.; Baghaei, M.; Prakash, B.; Mellibovsky, F.: Fluidic oscillators, feedback channel effect under compressible flow conditions. Sensors. **21**, 5768 (2021). https://doi.org/10.3390/s21175768
9. Tritton, D.J.: Physical fluid dynamics. Springer, Netherlands, Dordrecht (1977) https://doi.org/10.1007/978-94-009-9992-3
10. Portillo, D.J.; Hoffman, E.N.; Garcia, M.; LaLonde, E.; Hernandez, E.; Combs, C.S.; Hood, L.: Modal analysis of a sweeping jet emitted by a fluidic oscillator. In: AIAA AVIATION 2021 FORUM, American Institute of Aeronautics and Astronautics, Reston, Virginia, (2021). https://doi.org/10.2514/6.2021-2835.
11. Shmilovich, A.; Yadlin, Y.; Whalen, E.A.: Active flow control computations: from a single actuator to a complete airplane. AIAA J. **56**, 4730–4740 (2018). https://doi.org/10.2514/1.J056307
12. Koklu, M.: Effects of sweeping jet actuator parameters on flow separation control. AIAA J. **56**, 100–110 (2018). https://doi.org/10.2514/1.J055796
13. Andino, M.Y.; Lin, J.C.; Washburn, A.E.; Whalen, E.A.; Graff, E.C.; Wygnanski, I.J.: Flow separation control on a full-scale vertical tail model using sweeping jet actuators. In: 53rd AIAA Aerospace Sciences Meeting, (2015). https://doi.org/10.2514/6.2015-0785.
14. Melton, L.P.; Koklu, M.; Andino, M.; Lin, J.C.: Active flow control via discrete sweeping and steady jets on a simple-hinged flap. AIAA J. (2018). https://doi.org/10.2514/1.J056841
15. Xia, L.; Hua, Y.; Zheng, J.G.: Numerical investigation of flow separation control over an airfoil using fluidic oscillator. Phys. Fluids (2021). https://doi.org/10.1063/5.0047603
16. Arote, A.; Bade, M.; Banerjee, J.: Numerical investigations on stability of the spatially oscillating planar two-phase liquid jet in a quiescent atmosphere. Phys. Fluids (2019). https://doi.org/10.1063/1.5123762
17. Veerasamy, D.; Tajik, A.R.; Pastur, L.; Parezanović, V.: Effect of base blowing by a large-scale fluidic oscillator on the bistable wake behind a flat-back Ahmed body. Phys. Fluids (2022). https://doi.org/10.1063/5.0082844
18. Alikhassi, M.; Nili-Ahmadabadi, M.; Tikani, R.; Karimi, M.H.: A novel approach for energy harvesting from feedback fluidic oscillator. Int. J. Precision Eng. Manuf. -Green Technol. **6**, 769–778 (2019). https://doi.org/10.1007/s40684-019-00128-y
19. Hirsch, D.; Gharib, M.: Schlieren visualization and analysis of sweeping jet actuator dynamics. AIAA J. **56**, 2947–2960 (2018). https://doi.org/10.2514/1.J056776
20. Slupski, B.; Tajik, A.; Parezanović, V.; Kara, K.: On the impact of geometry scaling and mass flow rate on the frequency of a sweeping jet actuator. FME Trans. **47**, 599–607 (2019). https://doi.org/10.5937/fmet1903599S
21. Agricola, L.; Hossain, M. A.; Ameri, A.; Gregory, J. W.; Bons, J. P.: Turbine vane leading edge impingement cooling with a sweeping jet. In: Volume 5A: Heat Transfer, American Society of Mechanical Engineers, (2018). https://doi.org/10.1115/GT2018-77073.
22. Hossain, M.A.; Prenter, R.; Lundgreen, R.K.; Ameri, A.; Gregory, J.W.; Bons, J.P.: Experimental and numerical investigation of sweeping jet film cooling. J. Turbomach. (2018). https://doi.org/10.1115/1.4038690
23. Kim, D.; Yi, S.J.; Kim, H.D.; Kim, K.C.: Simultaneous measurement of temperature and velocity fields using thermographic phosphor tracer particles. J. Vis. **20**, 305–319 (2017). https://doi.org/10.1007/s12650-016-0394-2
24. Xu, Y.; Moon, C.; Wang, J.-J.; Penyazkov, O.G.; Kim, K.C.: An experimental study on the flow and heat transfer of an impinging synthetic jet. Int. J. Heat Mass Transfer **144**, 118626 (2019). https://doi.org/10.1016/j.ijheatmasstransfer.2019.118626
25. Mohammadshahi, S.; Samsam-Khayani, H.; Kim, K.C.: Experimental investigation on flow characteristics of compressible oscillating jet. Phys. Fluids (2022). https://doi.org/10.1063/5.0076544
26. Khan, T.I.; Tajik, A.R.; Parezanovic, V.: Drag reduction of a generic transport vehicle model using a fluidic oscillator. Int. J. Thermofluids **15**, 100180 (2022). https://doi.org/10.1016/j.ijft.2022.100180
27. Chen, X.; Zhong, S.; Ozer, O.; Weightman, A.: Drag reduction of a slanted-base cylinder using sweeping jets. Phys. Fluids (2022). https://doi.org/10.1063/5.0118386
28. Raman, G.; Raghu, S.: Miniature fluidic oscillators for flow and noise control: Transitioning from macro to micro fluidics. In: Fluids 2000 Conference and Exhibit, (2000). https://doi.org/10.2514/6.2000-2554.
29. Ramezanizadeh, M.; Alhuyi Nazari, M.; Ahmadi, M.H.; Chau, K.W.: Experimental and numerical analysis of a nanofluidic thermosyphon heat exchanger. Eng. Appl. Comput. Fluid Mech. **13**(1), 40–47 (2019). https://doi.org/10.1080/19942060.2018.1518272
30. Akbarian, E.; Najafi, B.; Jafari, M.; Faizollahzadeh Ardabili, S.; Shamshirband, S.; Chau, K.: Experimental and computational fluid dynamics-based numerical simulation of using natural gas in a dual-fueled diesel engine. Eng. Appl. Comput. Fluid Mech. **12**, 517–534 (2018). https://doi.org/10.1080/19942060.2018.1472670
31. Ghalandari, M.; Mirzadeh Koohshahi, E.; Mohamadian, F.; Shamshirband, S.; Chau, K.W.: Numerical simulation of nanofluid flow inside a root canal. Eng. Appl. Comput. Fluid Mech. **13**, 254–264 (2019). https://doi.org/10.1080/19942060.2019.1578696
32. Hussain, L.; Khan, M.M.; Ahmad, N.: Flow performance enhancement of a fluidic oscillator through the integration of rectangular ribs on Coanda surface. J. Fluids Eng. (2024). https://doi.org/10.1115/1.4065403
33. Tajik, A.R.; Kara, K.; Parezanović, V.: Sensitivity of a fluidic oscillator to modifications of feedback channel and mixing chamber geometry. Exp. Fluids **62**, 250 (2021). https://doi.org/10.1007/s00348-021-03342-0
34. Oz, F.; Kara, K.: Jet oscillation frequency characterization of a sweeping jet actuator. Fluids **5**, 72 (2020). https://doi.org/10.3390/fluids5020072
35. Yang, J.; Zhang, X.; Luo, Y.; Tang, L.; Liang, B.: Numerical parametric study of a sweeping-vortex low-frequency fluidic oscillator. Int. J. Mech. Sci. **271**, 109115 (2024). https://doi.org/10.1016/j.ijmecsci.2024.109115
36. Serrar, A.; El Khlifi, M.; Kourta, A.: Characterisation and comparison of unsteady actuators: a fluidic oscillator and a sweeping jet.

Int. J. Numer. Methods Heat Fluid Flow. **32**, 1237–1254 (2022). https://doi.org/10.1108/HFF-07-2021-0474
37. Joulaei, A.; Nili-Ahmadabadi, M.; Ha, M.Y.: Numerical study of the effect of geometric scaling of a fluidic oscillator on the heat transfer and frequency of impinging sweeping jet. Appl. Therm. Eng. **221**, 119848 (2023). https://doi.org/10.1016/j.applthermaleng.2022.119848
38. Meng, Q.; Du, X.; Chen, S.; Wang, S.: Numerical study of dual sweeping jet actuators for corner separation control in compressor cascade. J. Therm. Sci. **30**, 201–209 (2021). https://doi.org/10.1007/s11630-019-1231-4
39. Chen, S.; Li, W.; Meng, Q.; Zhou, Z.; Wang, S.: Effects of a sweeping jet actuator on aerodynamic performance in a linear turbine cascade with tip clearance. Proc. Inst. Mech. Eng. Part G J. Aerosp. Eng. **233**, 4468–4481 (2019). https://doi.org/10.1177/0954410018823606
40. Chen, X.; Zhong, S.; Ozer, O.; Weightman, A.: Control of afterbody vortices from a slanted-base cylinder using sweeping jets. Phys. Fluids (2022). https://doi.org/10.1063/5.0094565
41. Wen, X.; Li, Z.; Zhou, L.; Yu, C.; Muhammad, Z.; Liu, Y.; Wang, S.; Liu, Y.: Flow dynamics of a fluidic oscillator with internal geometry variations. Phys. Fluids (2020). https://doi.org/10.1063/5.0012471
42. Li, S.; Liu, Y.; Li, H.; Omidi, M.: Numerical study of the improvement in stability and performance by use of a partial vaned diffuser for a centrifugal compressor stage. Appl. Sci. **11**, 6980 (2021). https://doi.org/10.3390/app11156980
43. Kara, K.: Numerical study of internal flow structures in a sweeping jet actuator. In: 33rd AIAA Applied Aerodynamics Conference, American Institute of Aeronautics and Astronautics, Reston, Virginia, (2015). https://doi.org/10.2514/6.2015-2424.
44. Nili-Ahmadabadi, M.; Cho, D.-S.; Kim, K.C.: Design of a novel vortex-based feedback fluidic oscillator with numerical evaluation. Eng. Appl. Comput. Fluid Mech. **14**, 1302–1324 (2020). https://doi.org/10.1080/19942060.2020.1826360
45. Dong, Q.-L.; Xu, H.-Y.; Ye, Z.-Y.: Numerical investigation of unsteady flow past rudimentary landing gear using DDES, LES and URANS. Eng. Appl. Comput. Fluid Mech. **12**, 689–710 (2018). https://doi.org/10.1080/19942060.2018.1510791
46. Řidký, V.; Šidlof, P.; Vlček, V.: Numerical simulations of the flow with the prescribed displacement of the airfoil and comparison with experiment. EPJ Web of Conf. **45**, 1080 (2013). https://doi.org/10.1051/epjconf/20134501080
47. Mulu, B.G.; Cervantes, M.J.; Devals, C.; Vu, T.C.; Guibault, F.: Simulation-based investigation of unsteady flow in near-hub region of a Kaplan turbine with experimental comparison. Eng. Appl. Comput. Fluid Mech. **9**, 139–156 (2015). https://doi.org/10.1080/19942060.2015.1004816
48. Gritskevich, M.S.; Garbaruk, A.V.; Schütze, J.; Menter, F.R.: Development of DDES and IDDES formulations for the k-ω shear stress transport model. Flow Turbul. Combust. **88**, 431–449 (2012). https://doi.org/10.1007/s10494-011-9378-4
49. Menter, F.R.: Two-equation eddy-viscosity turbulence models for engineering applications. AIAA J. **32**, 1598–1605 (1994). https://doi.org/10.2514/3.12149
50. Vatsa, V.; Koklu, M.; Wygnanski, I.: Numerical simulation of fluidic actuators for flow control applications. In: 6th AIAA Flow Control Conference, American Institute of Aeronautics and Astronautics, Reston, Virigina, (2012). https://doi.org/10.2514/6.2012-3239.
51. Giles, M.B.; Pierce, N.A.: An introduction to the adjoint approach to design. Flow Turbul. Combust. **65**, 393–415 (2000). https://doi.org/10.1023/A:1011430410075
52. Marta, A.C.; Mader, C.A.; Martins, J.R.R.A.; Van der Weide, E.; Alonso, J.J.: A methodology for the development of discrete adjoint solvers using automatic differentiation tools. Int. J. Comput. Fluid Dyn. **21**, 307–327 (2007). https://doi.org/10.1080/10618560701678647
53. Baghaei, M.; Bergada, J.M.: Analysis of the forces driving the oscillations in 3D fluidic oscillators. Energies (2019). https://doi.org/10.3390/en12244720